AGU PUBLICATIONS

Journal of Advances in Modeling Earth Systems

RESEARCH ARTICLE

10.1002/2014MS000363

Key Points:
- A new synoptic-resolving CESM simulation has been performed for 100 years
- Good representation of Tropical sea surface temperature
- Realistic levels of El-Niño Southern Oscillation variability

Supporting Information:
- Readme
- Supplementary Text
- Supplementary Figures

Correspondence to:
R. J. Small,
jsmall@ucar.edu

Citation:
Small, R. J., et al. (2014), A new synoptic scale resolving global climate simulation using the Community Earth System Model, *J. Adv. Model. Earth Syst.*, *6*, 1065–1094, doi:10.1002/2014MS000363.

Received 14 JUL 2014
Accepted 22 OCT 2014
Accepted article online 28 OCT 2014
Published online 2 DEC 2014

A new synoptic scale resolving global climate simulation using the Community Earth System Model

R. Justin Small[1], Julio Bacmeister[1], David Bailey[1], Allison Baker[2], Stuart Bishop[1], Frank Bryan[1], Julie Caron[1], John Dennis[2], Peter Gent[1], Hsiao-ming Hsu[1], Markus Jochum[3], David Lawrence[1], Ernesto Muñoz[1], Pedro diNezio[4], Tim Scheitlin[2], Robert Tomas[1], Joseph Tribbia[1], Yu-heng Tseng[1], and Mariana Vertenstein[1]

[1]Climate and Global Dynamics Division, National Center for Atmospheric Research, Boulder, Colorado, USA, [2]Computational and Information Systems Lab, National Center for Atmospheric Research, Boulder, Colorado, USA, [3]Climate and Geophysics, Niels Bohr Institute, University of Copenhagen, Copenhagen, Denmark, [4]International Pacific Research Center, School of Ocean and Earth Science and Technology, University of Hawaii, Honolulu, Hawaii, USA

Abstract High-resolution global climate modeling holds the promise of capturing planetary-scale climate modes and small-scale (regional and sometimes extreme) features simultaneously, including their mutual interaction. This paper discusses a new state-of-the-art high-resolution Community Earth System Model (CESM) simulation that was performed with these goals in mind. The atmospheric component was at 0.25° grid spacing, and ocean component at 0.1°. One hundred years of "present-day" simulation were completed. Major results were that annual mean sea surface temperature (SST) in the equatorial Pacific and El-Niño Southern Oscillation variability were well simulated compared to standard resolution models. Tropical and southern Atlantic SST also had much reduced bias compared to previous versions of the model. In addition, the high resolution of the model enabled small-scale features of the climate system to be represented, such as air-sea interaction over ocean frontal zones, mesoscale systems generated by the Rockies, and Tropical Cyclones. Associated single component runs and standard resolution coupled runs are used to help attribute the strengths and weaknesses of the fully coupled run. The high-resolution run employed 23,404 cores, costing 250 thousand processor-hours per simulated year and made about two simulated years per day on the NCAR-Wyoming supercomputer "Yellowstone."

1. Introduction

The current generation of coupled general circulation models (CGCMs) is designed to be able to perform century and multicentury simulations and ensembles. With existing computing power availability, this has restricted models to have grid spacings of around or greater than 1° (∼100km). These models adequately resolve large-scale modes of climate variability (such as El-Niño Southern Oscillation (ENSO), Pacific Decadal Oscillation, North Atlantic Oscillation) but do not capture smaller-scale features such as Tropical Cyclones, mesoscale storms forced by steep orography, polar lows, ocean eddies, and fronts, which have important local impacts and may feedback to the large-scale climate. For example, for future climate simulations, it would be useful to know how the statistics of strong mesoscale storms such as Tropical Cyclones are projected to change in time.

Several different approaches have been applied to investigate the smaller-scale features of climate. Regional downscaling is a computationally efficient method of estimating the effect of large scales on smaller scales, but it cannot include the feedback to the larger scales. Mesh refinable global grids offer promise to allow "zooming" to small scale whilst including all the scale interactions, but require more knowledge of how to make parameterizations act across the different scales. Two-way nested grids embedded in a CGCM are a variation on this which also suffers from similar questions of how to treat eddies crossing boundaries from fine grid cells to coarser cells. Finally, globally high-resolution models include all the advantages of the above methods and none of their disadvantages, but are limited by computing power and data storage.

The new high-resolution global climate simulation presented here was enabled by an early use phase of the NCAR-University of Wyoming Supercomputer Center (NWSC). Such a simulation can potentially act as a benchmark for the other modeling approaches listed above. It can also be used to study climate interactions at all scales down to ocean mesoscale (tens of kilometers) and atmospheric mesoscale (hundreds of

kilometer). We could consider this as another (spatial) aspect of seamless weather and climate simulation [c.f. *Palmer et al*., 2008; *Hoskins*, 2013].

Previous high-resolution global simulations have revealed processes not seen in their low-resolution counterparts. A noncomprehensive list of examples is given next. *McClean et al*. [2011] showed examples of Tropical cyclones inducing cold wakes on the ocean surface, which can potentially affect storm strength (especially for slow moving storms). Some of the long-standing SST biases in east-boundary regions are reduced (especially off California [*McClean et al*., 2011; *Delworth et al*., 2012]), due to improved coastal winds [*Gent et al*., 2010] and consequently more realistic surface currents and ocean upwelling. Ocean eddies, a significant part of global ocean heat transport, are better captured [*McClean et al*., 2011]. Fundamental aspects of air-sea interaction are different when an eddy-resolving ocean model is included, with a dominant forcing of the atmosphere by the ocean at small scales [*Bryan et al*., 2010; *Kirtman et al*., 2012]. Some precipitation patterns over land show closer agreement with observations [*Delworth et al*., 2012], partly due to more realistic orography, in a similar manner to that found with regional downscaling. Aspects of the ITCZ bias are improved [*Delworth et al*., 2012], and other studies have shown ENSO to be better simulated at high resolution [*Shaffrey et al*., 2009; *Sakamoto et al*., 2012].

Despite these advances made with high-resolution global models, some problems remain or are exacerbated at these resolutions. For example, the ITCZ in the CESM class of models gets overstrong at high resolution in the atmosphere. Tuning is expensive at high resolution, so some simulations have exhibited too much warming or cooling with an especially notable effect on the polar regions where sea ice can be too thin and limited in area [*Kirtman et al*., 2012] or too thick and extensive [*McClean et al*., 2011], respectively.

The aim of this paper is to determine the improvements, degradations, and newly resolved aspects in global climate simulation that are found in the latest version of the CESM, at high resolution, relative to simulations with a more standard resolution of 1°, and also with previous high-resolution climate model runs. Specifically, we use Community Atmosphere Model (CAM) version 5 with the Spectral Element (SE) dynamical core, with grid spacing of 0.25°, in combination with the Parallel Ocean Program (POP2) with grid spacing of 0.1°. The particular foci are on small-scale events such as ocean eddies, Tropical cyclones, and orographically forced storms, on small-scale air-sea processes, and on large-scale features of the Tropical climate such as ENSO and the mean state of the Tropical Atlantic.

This is believed to be the longest run to date with CAM5-SE at 0.25° (coupled or uncoupled). The 100 year run allows for investigation of interannual variability and some decadal analysis. Data from the run are available for analysis and are served to the public via the Earth System Grid (see Acknowledgments).

The paper is structured as follows. Section 2 describes the model, observations, methods, and computing environment. Section 3 discusses model drift and climatology. Section 4 focuses on Tropical processes, including seasonal cycle, ENSO variability, and Tropical Cyclones. Section 5 covers midlatitude variability, including mesoscale convective systems over land, cold air outbreaks over the ocean, and ocean variability on a range of time scales. This is followed by a discussion on the comparative performance of the model relative to other global high-resolution climate models, the existing deficiencies, and the way ahead. Finally, Summary and Future Work is presented.

2. Models, Experiments, and Computational Performance

2.1. Model

The Community Earth System Model (CESM) [*Hurrell et al*., 2013] is a new generation climate model that succeeds the Community Climate System Model version 4 [*Gent et al*., 2011]. The model configuration used here has CAM5 [*Neale et al*., 2010] with a spectral element (SE) dynamical core [*Mishra et al*., 2011; *Dennis et al*., 2012], Community Ice Code version 4 [*Hunke and Lipscomb*, 2008], Parallel Ocean Program version 2 (POP2) [*Smith et al*., 2010], and Community Land Model version 4 [*Lawrence et al*., 2011].

As summarized in *Meehl et al*. [2013, and references therein], CAM5 includes new boundary layer, shallow convection, radiation, and microphysics schemes, as well as fully interactive aerosols. Amongst the improvements seen in CAM5 simulations (relative to the predecessor CAM4) are a better representation of cloud properties such as total cloud amount, optically thick cloud amount, and midlevel cloud [*Kay et al*., 2012; *Medeiros et al*., 2012], as well as reduced resolution dependence of certain fields such as short and

long-wave cloud forcing [*Bacmeister et al*., 2014]. In our simulation, CAM5 has a horizontal resolution of about 0.25° and the standard 30 levels in the vertical, with a model top of 3 hPa.

The POP2 model had a nominal grid spacing of 0.1° (decreasing from 11 km at the Equator to 2.5 km at high latitudes) in a tripole grid with poles in North America and Asia. The configuration was similar to that used in *McClean et al*. [2011] and *Kirtman et al*. [2012], except that the number of vertical levels was increased from 42 to 62 with more levels in the main thermocline. The ocean communicated with the coupler every 6 h, providing updated sea surface temperature and receiving update fluxes, and the atmosphere communicated every 10 min. The coupler computes air-sea fluxes using the *Large and Yaeger* [2009] surface layer scheme. The land and sea ice models were run at the same resolution and grid as the atmosphere and ocean models, respectively.

The high-resolution CESM was run under "present-day" (year 2000) greenhouse gas conditions (fixed CO_2 concentration of 367 ppm). This was chosen so that direct comparisons could be made with recent-era observations of fine-scale and large-scale phenomena. The prognostic carbon-nitrogen cycle was not used in this simulation.

In the following, this simulation will be referred to as **CESM-H**igh Resolution (CESM-H).

2.2. Computational Performance

The simulation was run on the Yellowstone IBM supercomputer, located at the NCAR-Wyoming Supercomputing Center, Cheyenne, Wyoming. Yellowstone is a 1.5 petaflops high-performance computing system with 72,288 processor cores, 144.6 TB of memory. The Yellowstone HPC system is based on IBM's iDataPlex architecture with Intel Sandy Bridge processors.

The first 60 years of this CESM simulation was performed over a 3 month time period of the "Accelerated Scientific Discovery" period, on 23,404 cores and together with supporting experiments consumed 25 million CPU hours. It cost about 250 K core hours per simulated year. The simulation was more computationally intensive than many previous CCSM simulations with similar resolution [e.g., *McClean et al*., 2011], largely because of the computational cost of prognostic equations for aerosols in the new CAM5 model (in CAM4 aerosols were prescribed). Indeed, only the use of the highly scalable Spectral Element atmospheric dynamical core allowed this kind of simulation to be performed so efficiently [*Dennis et al*., 2012].

The core count was chosen to maximize the model throughput (in terms of number of model years that could be run in a single day), while also keeping the computational cost reasonable (so as not to adversely affect the number of model years completed). A throughput of two simulated model years per day was obtained by carefully load balancing between the model components, some of which can largely run simultaneously (e.g., the ocean and atmosphere), while others couple more frequently. The input/output for the run was substantial, adding approximately 6.5% overhead to the run, and generating approximately one terabyte of data per compute day.

2.3. Initial Conditions and Run Parameters

The ocean initial condition was derived from the *Gouretski and Koltermann* [2004] climatology of WOCE and other data. This comprises optimally analyzed gridded fields of temperature and salinity on a 0.5° grid. Optimal interpolation was performed on density surfaces to avoid production of artificial water masses in the gridded data and results in sharper horizontal gradients. Hydrostatic stability of the analyzed climatological density profiles is also imposed. A short (1 year) ocean-ice spin-up was then run, forced by boundary conditions from the Coordinated Ocean Reference Experiment (CORE) protocol [*Large and Yaeger*, 2009]. (Computational limitations at the very start of the ASD period limited the length of the spin-up). There followed the main coupled run, during which time only small changes were made to the model setup, in ice time step and coupling interval, ocean time step, and to the minimum snow thickness threshold, as well as processor layout.

2.4. Supporting Experiments

In addition to the main coupled experiment described above, two 7 year cycles of an atmosphere-only simulation with the same atmosphere model configuration and resolution were run using the daily 0.25° National Oceanographic and Atmospheric Administration (NOAA) Optimum Interpolation (OI) SST product

(OISST-0.25°) [*Reynolds et al*., 2007] as a surface boundary condition, each for years 2004–2010. This is referred to as **CESM-A**tmosphere (CESM-A).

A standard resolution equivalent to CESM-H was run for 166 years, for year 2000 conditions, and with no active Carbon-Nitrogen cycle. The CAM5-SE atmosphere and land grid were about 1°, and the ocean and ice models had nominal 1° spacing, (the actual spacing of POP is uniform at 1.125° in the zonal direction but varies from 0.27° in meridional direction at the equator, to around 0.5° at higher latitudes [*Danabasoglu et al*., 2006]). Initial conditions for ocean and ice are created in the same way as for the high-resolution case, but with the standard resolution ocean-ice model. The ocean and atmosphere communicated with the coupler every 6 h and 30 min, respectively.

This simulation will be will be referred to as **CESM-S**tandard Resolution (CESM-S). Note that comparisons are made between CESM-H and CESM-S only when strictly necessary and informative—in some cases, it is not appropriate to show standard resolution results (e.g., for Tropical Cyclones), whilst in other cases, more research is required to understand differences between the simulations.

During the course of the high-resolution simulation CESM-H, it was found that the 0.25° soil erodability map gave rise to a low dust aerosol burden (P.-L. Ma and P. Rasch, personal communication, 2013). Rather than rerun the expensive simulation, or modify the map and the dust burden mid-way through the run (at risk of changing the climate state in an unexpected fashion), the problem was investigated by running the standard resolution case with a variety of different dust burdens, including both realistic and low burdens. We found that changes to dust burden did not substantially alter the fields of interest to us in this paper. (A better quality soil erodability map is now standard with 0.25° CAM5.)

2.5. Model Tuning

For simulations of twentieth century climate and beyond, a common approach is to start the run with preindustrial greenhouse gas concentrations (typically 280 ppm), adjust the model parameters (via "tuning") to achieve a small ($<$0.1 W m^{-2}) top of atmosphere (TOA) radiation imbalance, and then proceed forward with simulating the subsequent time period. This ensures some confidence that the subsequent changes in TOA imbalance are due to external forcing (i.e., increases in greenhouse gas) rather than inherent model imbalances.

This kind of approach is not feasible for high-resolution models, due to the computational expense of running long periods. Our approach for this "year 2000" simulation was simply to run mostly with parameter values developed for atmosphere-only simulations at the same resolution (particularly for CESM-H), or from coupled runs for preindustrial conditions (for CESM-S), and apply a minimal amount of new tuning.

For our simulations, some tuning was necessary, especially as the CESM has rarely been applied in a constant "year 2000" mode, and the standard model settings are previously adjusted based on preindustrial conditions. It may be argued that the use of tuning makes it hard to interpret differences in model solution as due to resolution alone, and indeed caution must be applied in the interpretation of model differences as such. In addition, the different ocean model resolutions employ different schemes and parameterizations (as discussed later), some related to the different resolution, but also because some schemes (e.g., latitudinally varying diffusivity, see section 4.1) have not been tested yet in the high-resolution version, which is generally less developed due to computational expense. The interpretation of the model data employed in this paper is that the CESM-H and CESM-S are the best simulations available at their respective resolutions, for the same model version, and for year 2000 conditions. More details of model setup and tuning are contained in supporting information Document 1.

3. Model Drift and Climatology

It has previously been suggested that high resolution can improve some aspects of model drift (e.g., reduced drift when ocean eddies are resolved [*Delworth et al*., 2012]), as well as model climatology (such as improved precipitation when orography is better resolved [*Delworth et al*., 2012]). This section discusses the new model drift and climatology and whether we see improvements due to resolution in CESM.

3.1. Model Drift

In the CESM-H simulation, the TOA radiation imbalance reduced reasonably quickly, from around 1 W m^{-2} at the beginning of the run to 0.5 W m^{-2} after 60 years, ending at around 0.3 W m^{-2} (Figure 1a, CESM-H is

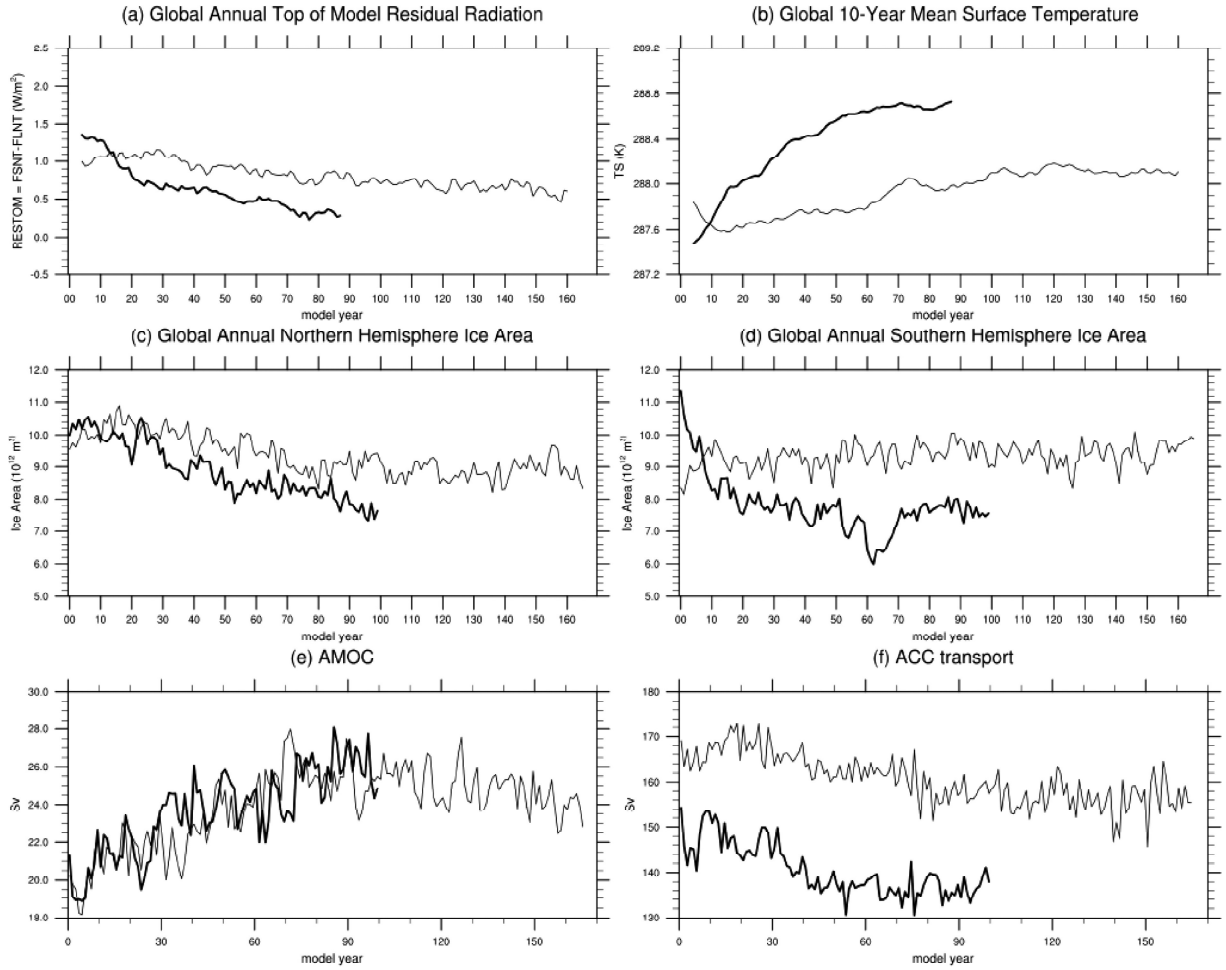

Figure 1. Time series of globally averaged quantities for 100 years of CESM-H (thick black line) and 166 years of CESM-S (thin gray line). (a) Top of atmosphere net radiation, positive incoming to Earth. Data are 10 year running mean. (b) Surface (including ocean, land, ice) temperature, 10 year running average. Sea ice area in (c) Northern Hemisphere and (d) Southern Hemisphere. (e) Atlantic Meridional Overturning Circulation (AMOC), 12 month running averages, (f) transport through Drake Passage due to Antarctic Circumpolar Current (ACC), annual values.

shown as black line in all plots). This evolution at constant year 2000 values of forcing seems reasonable given that current estimates of the TOA imbalances due to transient greenhouse gas forcing are around 0.5–1.0 W m^{-2} [*Hansen et al.*, 2005; *Trenberth et al.*, 2009; *Loeb et al.*, 2012; *Balmaseda et al.*, 2013, and references therein]. However, we cannot fully distinguish between inherent model imbalances and true global warming effect in the simulation. Note that our simulation was not planned for climate change studies, instead to simulate a period when reasonably extensive observations existed for model validation. The model TOA radiation imbalance compares well with previous high-resolution global model simulations which typically also achieve between 0.5 and 1 W m^{-2} [*Shaffrey et al.*, 2009; *Delworth et al.*, 2012; *Sakamoto et al.*, 2012].

The global surface temperature in CESM-H increases by 1.2°C over the whole 100 years (Figure 1b). Global sea surface temperature initially cools from the initial condition, and the first 15 years has a global mean difference of −0.64°C compared to HADISST present-day SST, but the surface ocean subsequently warms so that the corresponding difference is +0.21°C over years 60–90, with a suggestion of equilibriation toward the end of the run.

The Atlantic Meridional Overturning Circulation (AMOC), defined as maximum overturning streamfunction in Northern Hemisphere below 500 m depth, spins-up to about 20 Sv (1 Sv = 10^6 m^3 s^{-1}) in the 1 year of forced ocean-ice simulation (not shown) and then rises steadily through the 100 year coupled simulation of

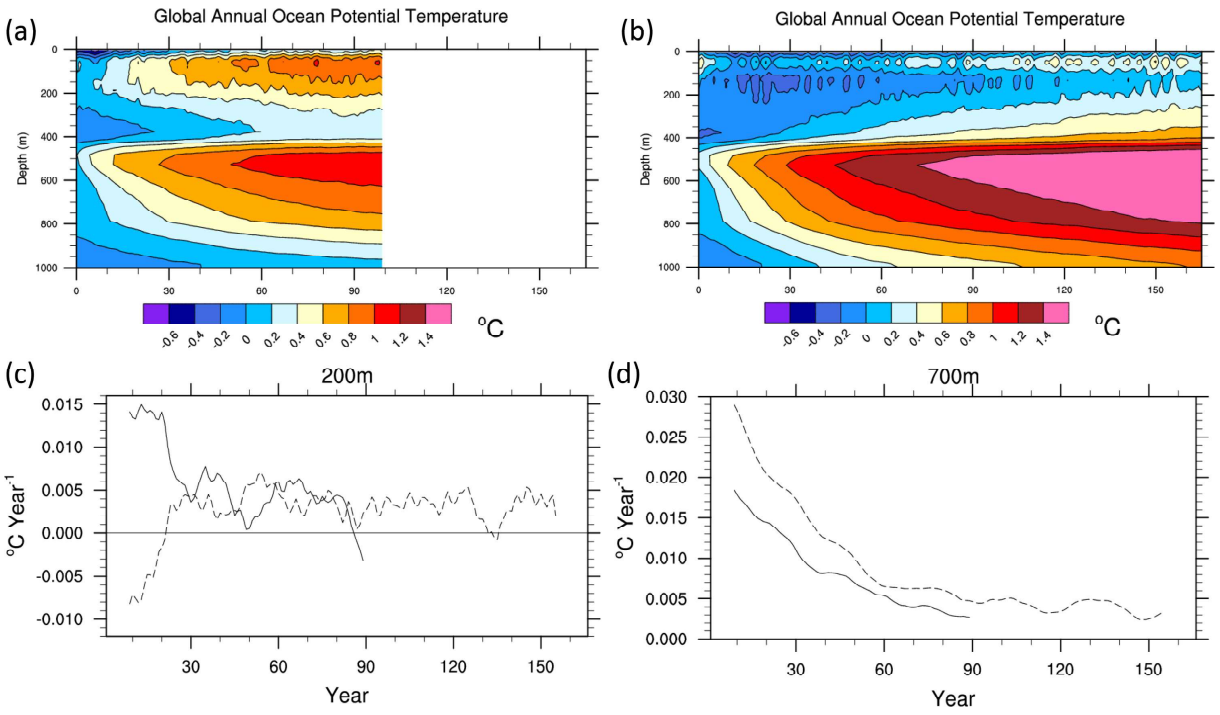

Figure 2. Globally averaged ocean potential temperature difference from initial condition, versus depth to 1000 m, for (a) CESM-H and (b) CESM-S. Time rate of change of temperature for CESM-H (solid) and CESM-S (dashed), at a depth of (c) 200 m and (d) 700 m. Data in Figures 2c and 2d have been smoothed twice with a 10 year running mean to remove effect of transients.

CESM-H, reaching 26 Sv at the end (Figure 1e), more than observed values of 18.7 $\pm$ 2.1 Sv from the Rapid Climate Change-Meridional Overturning Circulation and Heatflux Array [*Kunzow et al.*, 2010]. Transport through Drake Passage likewise quickly spins-up to nearly 150 Sv initially, before settling to values between 130 and 140 Sv (Figure 1f), favorably comparing with observed estimates of 136.7 $\pm$ 7.8 Sv [*Cunningham et al.*, 2003].

The global volume averaged ocean potential temperature in CESM-H rose by 0.165°C over the 100 year period. Much of the ocean warming takes place in the top 1000 m, especially at depths around 50–100 and 500–1000 m where the temperature increases by around 1°C over the 100 years (Figure 2a). Inspection of the interbasin distribution (not shown) revealed that much of the warming occurred in the subtropical gyres of the North and South Atlantic and North Pacific, as well as the Southern Ocean. Northward displacement of the main oceanic fronts (Gulf Stream and Kuroshio Extension) relative to observations, and anomalously warm Mediterranean Sea outflow, contributed to the warming.

Figures 1c and 1d show the annual mean sea ice area in CESM-H for both hemispheres. The ice area for the Northern Hemisphere shows a steady decline over the 100 year period, from 10.0 million km^2, ending at 7.5 million km^2. The Southern Hemisphere ice area initially rapidly reduces but appears to be well equilibrated after year 20 (except for a dip around year 60) and also reaches 7.5 million km^2. Ice volume shows similar trends ending at 1×10^{13} m^3 (0.7×10^{13} m^3) for the Northern and Southern Hemispheres, respectively (not shown). The mean sea ice area for both hemispheres starts out reasonably close to the satellite observations in the early part of the simulation, in contrast to previous CCSM4 high-resolution experiments [*McClean et al.*, 2011; *Kirtman et al.*, 2012], but drops to very low values later in the run, as discussed in section 3.2.

For reference, some relevant results from the CESM-S case are now discussed. The TOA radiation imbalance started at around 1 W m^{-2} and was approaching 0.5 W m^{-2} at the end of the 166 year run (Figure 1a, gray line), a much slower reduction than in the high-resolution run. The global averaged surface temperature stopped drifting upward and stabilized at around year 120 (Figure 1b). Likewise, the Northern Hemisphere sea ice area stabilized at about 9.0 million km^2 at around the same time (Figure 1c), and the Southern Hemisphere sea ice area stabilized much earlier, after the first 50 years, at 9.5 million km^2 (Figure 1d, see also Figure 5 below for the seasonal cycles of both of these runs).

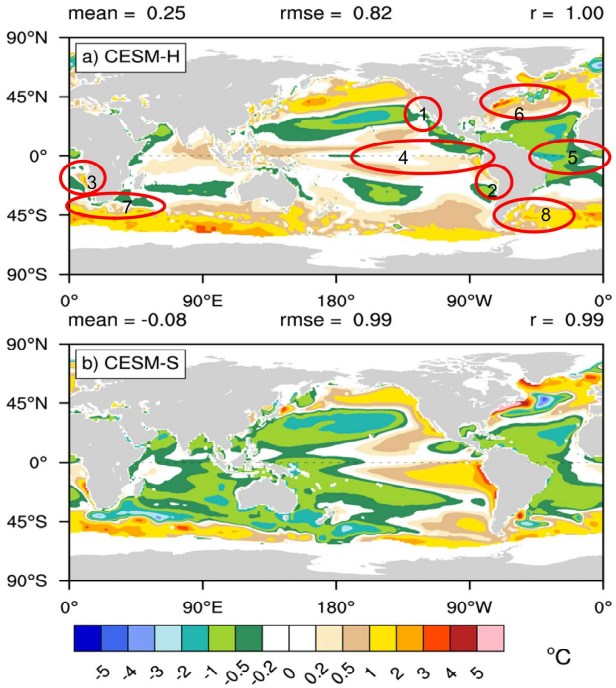

Figure 3. SST biases, for the annual climatological mean. (a) CESM-H and (b) CESM-S. Both are compared against "present-day" HADISST (1999–2008). Note nonlinear color scale. Areas referred to in text are circled in Figure 3a and numbered. The mean difference, spatial root mean square error, and spatial correlation for the model versus the HADISST climatology are shown at the top of each figure.

The AMOC follows a very similar upward trend in the first 100 years of CESM-S relative to CESM-H (Figure 1e), but after that it steadily reduces to around 24 Sv by the end of the run. Looking in more detail, the time series of the two runs are very close to around year 15, but thereafter exhibit considerable differences on interannual time scales (Figure 1e). Meanwhile Drake Passage transport values are much higher in CESM-S than in CESM-H, ranging from 170 to 150 Sv with a general weakening trend (Figure 1f). It will be shown later that wind stress in the Southern Ocean has a different structure in the two runs: strongest winds are located further equatorward in CESM-S compared to CESM-H.

As with CESM-H, there is considerable warming in the ocean subsurface in CESM-S, at depths of 500–800 m, but the temperatures in the top 200 m are less than in the former (Figure 2b). In terms of the rate of change of temperature, this is always positive at depths around 700 m, with CESM-S warming faster (Figure 2d), whilst at 200 m, the rate of change is generally positive in both runs after year 30 (Figure 2c). This indicates that globally both models warm in a similar fashion after the first few decades of transient response to initial conditions. The large rate of change of ocean temperature in CESM-S is in response to the larger TOA radiation imbalance (Figure 1a), with the excess heat warming the ocean rather than the sea ice and surface air temperature (Figures 1b–1d).

3.2. Climatology

Based on the model drift statistics discussed in the above section, model climatologies are formed from later parts of the simulations where the surface is more equilibriated: specifically years 60–90 for CESM-H and years 136–166 for CESM-S.

3.2.1. SST

The annual mean SST climatology of CESM-H is characterized by relatively small SST bias in the Tropics, a cool bias in the subtropics and warm bias in mid to high latitudes (Figure 3a), relative to the Hadley Centre sea ice and SST data set (HadISST) [*Hurrell et al*., 2008]. CESM-S also has a warm bias in the midlatitude Southern Ocean and cool bias in the subtropical North Atlantic and North Pacific (Figure 3b). However, there are a number of regions of substantial improvement in the high-resolution run, such that the spatial root-mean-square-error (RMSE) of model SST computed from the global map of Figure 3a is 0.82, compared to 0.99 in Figure 3b. The examples circled in Figure 3a are discussed next.

Warm SST biases in the eastern boundary regions are reduced (regions 1, 2, and 3). Similar results for the California current and Peru-Chile upwelling region were found by, e.g., *Gent et al*. [2010], *McClean et al*. [2011], and *Delworth et al*. [2012]. Improvement of the Benguela upwelling has been more difficult to achieve, with only *Gent et al*. [2010] showing a significant improvement, based on a change in atmospheric grid spacing from 2° to 1/2°. CESM-H shows a small SST bias (relative to CCSM4 with atmosphere at 2° to 1°) [*Gent et al*., 2011], but is comparable with CCSM4 with atmosphere at 1/2° [*Gent et al*., 2010]. The bias

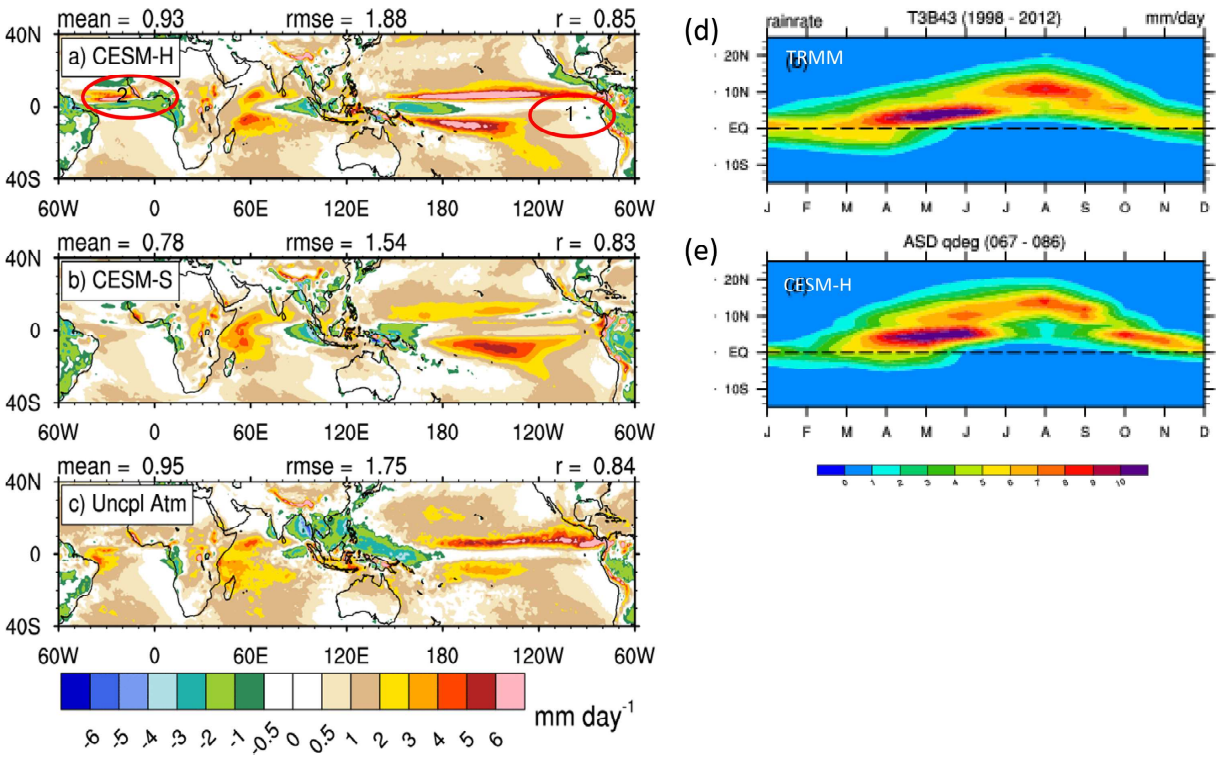

Figure 4. (a–c) Precipitation bias fields for annual mean climatology, relative to Tropical Rainfall Measurement Mission (TRMM). CESM-H (Figure 4a), CESM-S (Figure 4b), and uncoupled high-resolution atmosphere run CESM-A (Figure 4c). Areas discussed in text are circled in Figure 4a. (d and e) Precipitation seasonal cycle averaged between 10°W and 10°E, shown as a function of latitude from 15°S to 25°N. Figure 4d is a climatology from TRMM 3B43 product and Figure 4e is CESM-H. In Figures 4a–4c, the mean difference, spatial root mean square error, and spatial correlation for the model versus observations are shown at the top of each figure.

reduction occurs not just in the Benguela upwelling (region 3) but across the whole Tropical Atlantic where the bias turns mostly negative (region 5, Figure 3a). This is a slight improvement on CESM-S (Figure 3b), and a big improvement on the previous generation of the model, CCSM4, which had warm SST biases of 2°C or more along the equator east of 10°W [*Gent et al.*, 2011, Figure 1a]. This is discussed in more detail in section 4.1.

SST errors in western boundary currents such as the Gulf Stream and Brazil-Malvinas confluence (regions 6 and 8), and also in the Antarctic Circumpolar Current (e.g., region 7) are of lesser magnitude in CESM-H than in CESM-S (Figures 3a and 3b). At higher resolution the Gulf Stream still separates from the U.S. coast too far north and then extends more eastward than observed (Figure 3a), but the path and SST errors are substantially less than in CESM-S (Figure 3b) and compare favorably with previous high-resolution coupled simulations. There is also an improvement in SST in CESM-H just east of Hokkaido, Japan, due to better representation of the Kuroshio/Oyashio system, but this is countered by the generally warm midlatitude bias mentioned above. In the Southern Ocean, a strong dipole of cool/warm SST biases north/south of the ACC in CESM-S (Figure 3b) is replaced by a more gradual poleward warming tendency in CESM-H (Figure 3a).

Tropical, annual mean SST in the Pacific and Indian Ocean is quite well represented in CESM-H, with biases of less than 1°C (Figure 3a), which contrasts with too warm temperatures in the East Pacific in CESM-S (Figure 3b). In the central Tropical Pacific, warm SST bias brackets a cool bias along the equator in CESM-H and in CESM-S, which is often associated with double ITCZ problems, but with weaker magnitude in CESM-H than in many other climate model simulations [*Davey et al.*, 2002]. The Tropical Ocean characteristics will be examined in more detail in section 4.1.

3.2.2. Precipitation

The most prominent feature of the annual mean climatological precipitation field in the Tropics is that the northern ITCZ precipitation amount is too high in CESM-H (relative to multisensor products such as Tropical

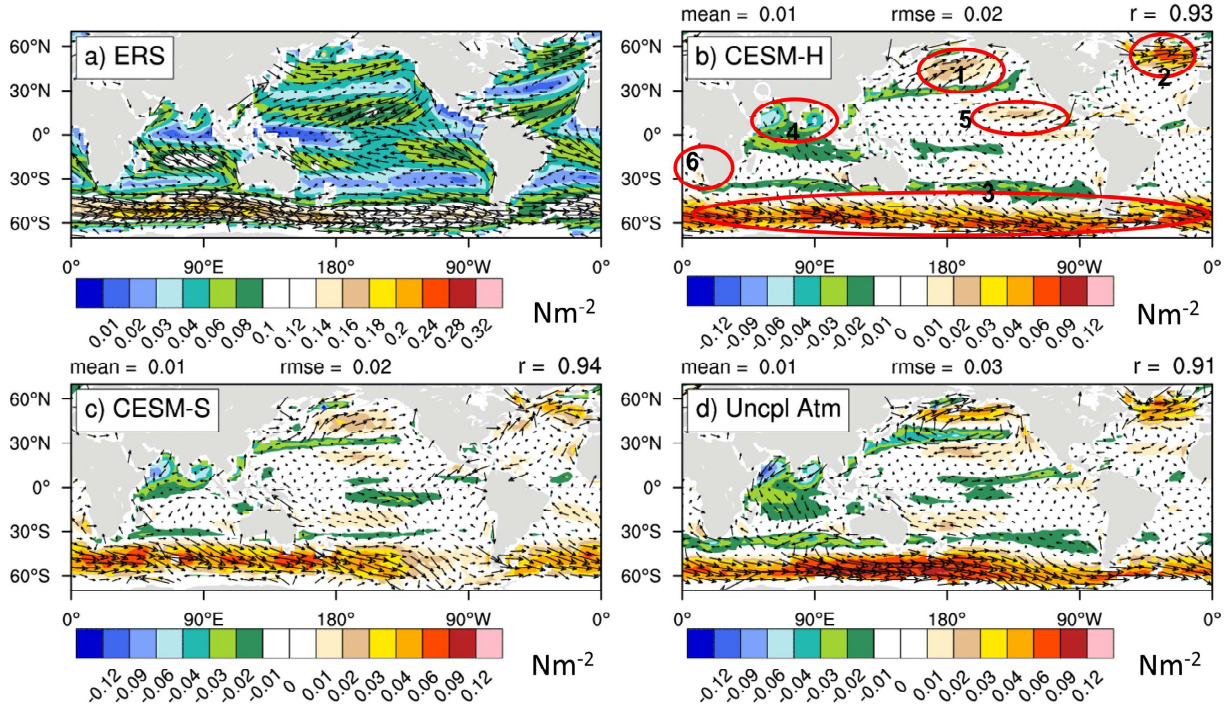

Figure 5. Surface wind stress (vectors) and magnitude of mean stress vector in color, annual mean climatology. (a) From European Remote Sensing (ERS) scatterometer. Difference between model run and ERS scatterometer (b) for CESM-H, (c) for CESM-S, and (d) for atmosphere-only run CESM-A. Areas discussed in text are circled in Figure 5b. The mean difference, spatial root mean square error, and spatial correlation for the model versus the ERS climatology are shown at the top of Figures 5b–5d.

Rainfall Measurement Mission (TRMM [*Huffman et al*., 2007]), shown here, and Global Precipitation Climatology Project, GPCP [*Huffman et al*., 1997]), and the South Pacific Convergence Zone is too strong and zonal (Figure 4a). However, the double ITCZ problem in the Far eastern Pacific is reduced with high resolution (region 1 of Figure 4a, compare with CESM-S in Figure 4b) and the excessive precipitation bias offshore of Ecuador/Colombia is also reduced. These results are similar to those obtained in *Delworth et al*. [2012].

The atmosphere component of CESM-H (i.e., CESM-A), when forced by observed, high-resolution SST, also exhibits excessive precipitation in the eastern Pacific ITCZ and in the Indian Ocean (Figure 4c). *Bacmeister et al*. [2014] have shown similar characteristics of CAM5 using a Finite Volume dynamical core at 0.25°. However, CESM-A has too little precipitation in the western Pacific warm pool (Figure 4c), and it is possible that the slight excess of precipitation there in CESM-H (Figure 4a) is due to locally warm SST (Figure 3a). CESM-H has a much narrower and more intense ITCZ than CESM-A in the central Pacific and in the Atlantic. The Atlantic ITCZ error in CESM-H (region 2, Figure 4a) is of fundamentally different character to that of CESM-S (Figure 4b) and CESM-A (Figure 4c), and represents a strengthening of the ITCZ but in the correct location. This point will be returned to in section 4.1.

An example of a seasonal cycle of precipitation that is well captured is the monsoon over West Africa, whose importance has been stressed during recent decades [e.g., *Cook et al*., 2012, and references therein]. The monthly climatology of precipitation in TRMM averaged between 10°W and 10°E shows the strong rainfall between April and June a few degrees north of the Equator (Figure 4d) then a monsoon "jump" around June and July in the neighborhood of 5°N. *Cook et al*. [2012] have previously shown that the CCSM4 West African monsoon makes the jump at the right time (June and July), but the early season rainfall is south of the equator, related to a large warm SST bias there. The CESM-H simulation (Figure 4e) indicates significant improvement over CCSM-4 in simulating the earlier rain band both in intensity and location (north of the Equator, at about 5°N).

3.2.3. Winds Over the Ocean

A notable feature of CAM5 (and predecessors) is that the winds in extratropical storm tracks are too strong, resulting in excessive time-mean wind stress over the ocean in CESM-H (Figure 5b, regions 1–3). This aspect

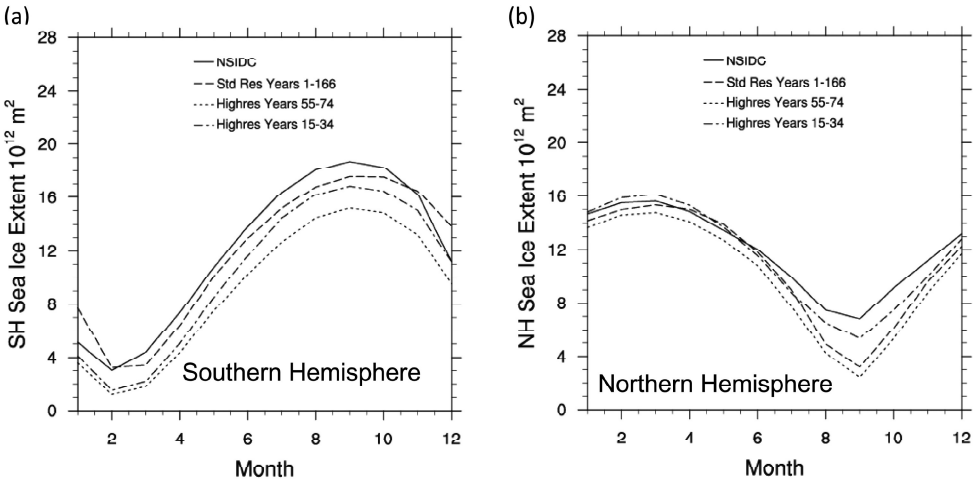

Figure 6. Northern and Southern Hemisphere sea ice extent, seasonal cycle. (a) Southern Hemisphere and (b) Northern Hemisphere. Dotted and chained lines denote CESM-H, for years 15–34 and 55–74, respectively. Solid black line is interpretation of observations from National Snow and Ice Data Center (NSIDC), and the dashed line is a long-term average from CESM-S.

is also present in the associated high-resolution atmosphere-only CESM-A (Figure 5d) and CESM-S (Figure 5c). In contrast, winds are too weak in the Indian monsoon region (Figure 5b, region 4, Figures 5c and 5d). In the eastern equatorial Pacific, the trade winds are too strong in CESM-H (Figure 5b, region 5) and CESM-A (Figure 5d) simulations.

Relative to CESM-S (Figure 5c), CESM-H has a southward shifted wind stress bias in the Southern Ocean (Figure 5b, region 3), particularly in the South Indian sector. There is an improvement under higher resolution in the wind stress in the south-east Atlantic, on the eastern edge of the subtropical high (compare Figure 5b, region 6, with Figure 5c) where the offshore wind jet is reduced to more realistic values. The wind bias is most pronounced in CESM-S in DJF and occurs well away from the coast, and thus does not have a direct effect on coastal upwelling (see also discussion in section 4.1, Atlantic).

3.2.4. Sea Ice

A long-standing problem with the CCSM family of models was the overestimation of sea ice in the Southern Hemisphere. To some extent this was improved in previously performed standard resolution CESM simulations, except that the model Austral summer ice extent was still much too high. The difficulty in simulating the seasonal cycle arises in the November-December and December-January transition, when the real Southern Ocean sea ice experiences a very rapid retreat (Figure 6a, solid line).

The standard resolution CESM-S slightly underestimates winter Austral sea ice, compared to long-term (1981–2005) observations from the National Snow and Ice data Center (NSIDC), but still has too much Austral summer ice (Figure 6a, dashed line). The model rapid transition is weaker than observed in November-December, and instead occurs strongly in January to February whilst the minimum extends into March (Figure 6a, dashed), a time when the real winter sea ice advance begins.

The high-resolution simulation CESM-H experiences gradual ice loss (as in Figures 1c and 1d) through the run, especially in the Southern Hemisphere in Austral winter through early summer (Figure 6a, dotted and chained lines) and in the Northern Hemisphere in Boreal summer (Figure 6b). However, the shape of the annual cycle of Southern Hemisphere sea-ice extent is somewhat improved, with a more rapid reduction between November and December, a minimum in February, then an advance by March (Figure 6a).

The simulations of Northern Hemisphere sea ice are more similar between CESM-H and CESM-S when the later, more equilibriated, part of the high-resolution run is used (Figure 6b, dotted and dashed lines). The models show notably less Boreal summer minimum sea-ice compared to the "current average" (1981–2005) observed values of 7.5 million km^2, with CESM-S having 3 million km^2 and CESM-H 2.5 million km^2 (Figure 6b). To place these persistent year 2000 simulations in context, the observed September minimum sea ice extent from NSIDC for 2007 and 2012 (the record minimum years) was around 4.3 million km^2 and 3.4

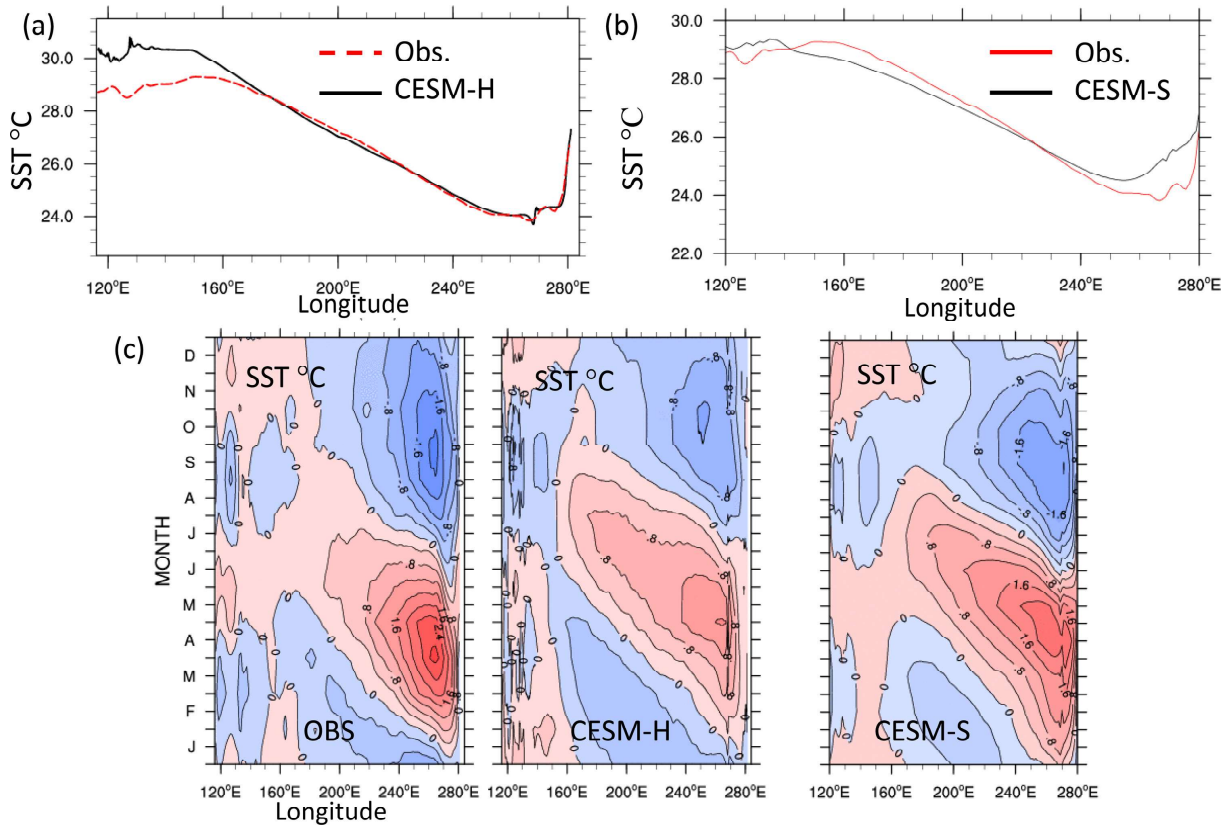

Figure 7. (a) Annual mean SST along the Equator, Pacific Ocean. Black line: CESM-H, red line: *Reynolds et al.* [2002] climatology. (b) As Figure 7a but for CESM-S. Data are averaged between latitudes 1.5°S and 1.5°N. (c) Seasonal cycle of SST at equator from (left) Reynolds et al. climatology, (middle) CESM-H, and (right) CESM-S.

million km^2, respectively, whilst the CESM scenario runs of *Meehl et al.* [2013] show August-September-October (ASO) sea ice reducing to around 3.5 million km^2 in the 21st century in RCP 2.6, a low emission scenario which led to CO_2 concentrations of between 400 and 500 ppt.

4. Tropical Characteristics

The Tropics is a region where high resolution has previously been suggested to be important for climate modeling. For example, *Roberts et al.* [2009] found improved eastern Pacific ocean temperature when Tropical Instability Waves are resolved, and a better simulation of ENSO was obtained by *Sakamoto et al.* [2012] and *Delworth et al.* [2012] in high-resolution models. Here we discuss the mean state, and annual cycle of the Tropical Pacific and Atlantic, as well as Tropical variability such as ENSO, Madden-Julian-Oscillation, and Tropical Cyclones, in our simulations.

4.1. Mean State and Annual Cycle

4.1.1. Pacific Ocean

The small SST bias in the equatorial Pacific in CESM-H (Figure 3a) is emphasized quite clearly by the zonal SST along the Equator, which is within 0.2°C of observations east of 160°E (Figure 7a). However, over the maritime continent west of 160°E, SST is up to 1.5°C warmer than observed, whilst CESM-S has a much smaller bias (Figures 7a and 7b). CESM-S has a weaker zonal SST gradient, with surface temperature too warm by up to 1.5°C in the east, and too cold by 0.5°–1°C at 160°E (Figure 7b). The latter is typical of many global models exhibiting warm waters extending from the Peru/Chile coast, and a too-cold cold tongue extending too far west [*Davey et al.*, 2002].

The seasonal cycle of equatorial SST along the equator shows westward propagation in both CESM-H and observations (Figure 7c, left and middle), but the model amplitude is too weak, with a delayed start

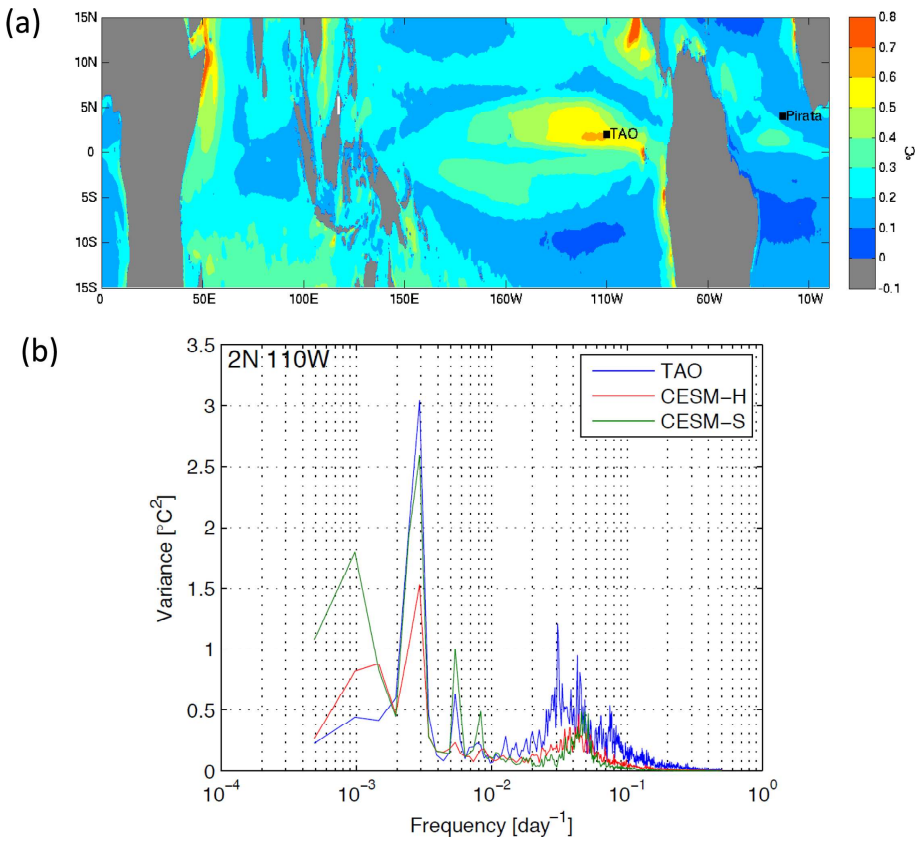

Figure 8. (a) SST standard deviation from CESM-H data filtered to show sub-90 day variability. Squares show locations of a Tropical Atmosphere Ocean (TAO) mooring at 110°W, 2°N and a PIRATA mooring at 23°W, 4°N. (b) Variance spectra of unfiltered daily SST at location of TAO mooring, from CESM-H (red), CESM-S (green), and TAO (blue).

(by ∼ 1 month) of warm anomalies in boreal Spring and cold anomalies in boreal Fall. The westward propagation is related to the seasonal cycle in wind stress, coupled atmosphere-ocean processes, and ocean dynamics [*Chang*, 1994; *Dijkstra and Neelin*, 1995; *Yu and McPhaden*, 1999]. CESM-S has slightly better phase and amplitude of the seasonal cycle (Figure 7c, right).

One of the proposed reasons for improved annual-mean eastern equatorial Pacific SST structure at high resolution, and for reducing the common too-cold cold tongue bias, is that the effect of Tropical Instability Waves (TIWs) in fluxing heat toward the Equator is well simulated [*Jochum et al*., 2008; *Roberts et al*., 2009]. We do not attempt a detailed heat budget here, but note that a map of the standard deviation of high-pass filtered SST from CESM-H shows that in the Pacific TIWs are prominent (Figure 8a, compare with Figure 1b of *Small et al*. [2005]), although a comparison with TOGA TOA mooring data reveals the SST variance is smaller than observed in the 10–50 day period band (Figure 8b).

The CESM-H model TIW's surface eddy kinetic energy (EKE) compares well with the TAO array record at 140°W (not shown), suggesting that the weak SST variance is not the result of insufficiently resolved dynamics, but rather the result of not adequately represented thermodynamic processes that affect the SST. In particular, TIWs create vertical shear that leads to Kelvin-Helmholtz instabilities and vertical mixing, a process that in the present model is not resolved but only parameterized [see *Jochum and Murtugudde*, 2006]. Furthermore, TIWs directly affect surface winds and air-sea heat flux [*Chelton et al*., 2004], and long and short-wave radiation by inducing cloud formation [*Deser et al*., 1993]. Either one of these processes could be poorly represented and lead to a bias in the SST variance, even if the TIW dynamics are represented quite well.

A common feature of global climate models is that the Equatorial thermocline is too deep and too diffuse when compared with observations, partly related to high values of the background thermocline diffusivity.

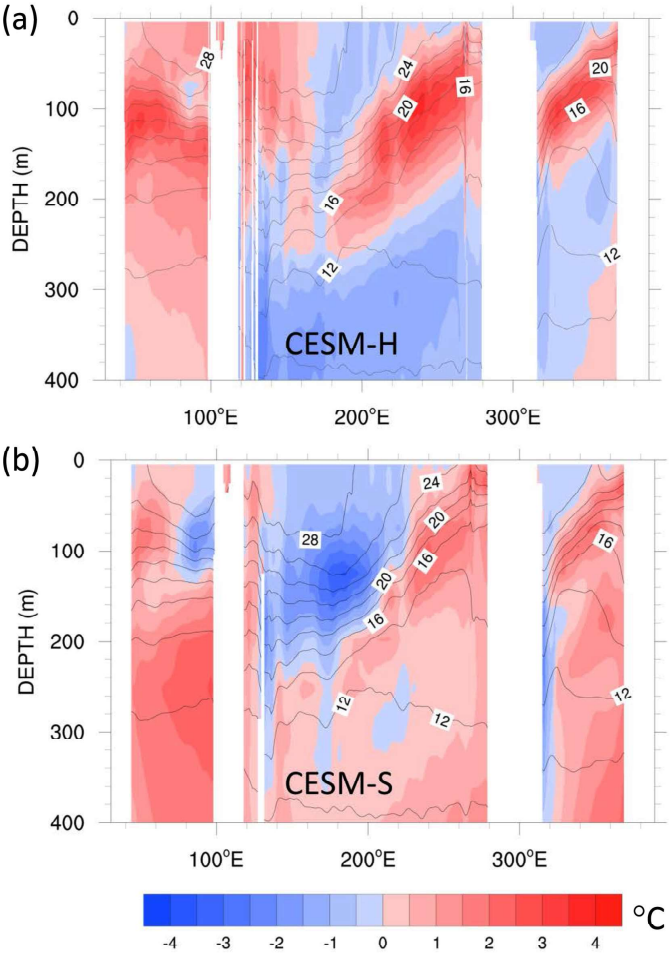

Figure 9. Vertical section of annual-mean potential temperature versus longitude at the Equator, differenced against *Levitus et al.* [1998] climatology of observations: (a) CESM-H and (b) CESM-S. Light contour intervals are 1°C, and negative/positive differences are in shades of blue/red, respectively. Levitus climatology is overlaid as dark black contours.

As described by *Jochum* [2009], a latitudinally varying diffusivity was introduced to standard resolution POP to mimic observations of reduced diffusivity at the Equator [*Gregg et al.*, 2003] as well as higher latitude variations in diffusivity. Vertical diffusivity in an OGCM represents the mixing caused by breaking internal waves, a process that cannot be resolved by OGCMs. Ideally, it would depend on the model state, like stratification or levels of turbulent kinetic energy [e.g., *Osborn*, 1980], but the observational and theoretical knowledge is insufficient to constrain any sophisticated parameterization [e.g., *MacKinnon*, 2013].

Introduction of a latitudinally varying diffusivity led to some improvement in the Equatorial thermocline and the energy associated with TIWs in standard resolution CESM, but it still placed the thermocline too deep and had a weak vertical gradient compared to observations [*Jochum*, 2009]. In CESM-S, which uses this scheme, the problem is manifested by 2°C temperature biases at around 100 m in the eastern equatorial Pacific (Figure 9b). Note however cool temperature biases in the western Pacific at these depths, indicating that the zonal slope of the thermocline is too weak.

In CESM-H, the spatially dependent diffusivity was not yet implemented. This may explain why the subsurface temperature bias in the CESM-H case is larger than in CESM-S, reaching 3°C at 100 m in the eastern Equatorial thermocline, whilst the western Pacific also has a warm bias above 150 m (Figure 9a). The deep thermocline could be a factor in reducing the amplitude of the seasonal cycle of SST in the equatorial Pacific, as well as ENSO variability as discussed later. Further, the SST variance associated with TIWs in CESM-H is not much higher than that of CESM-S, a possible consequence of the lack of reduced diffusivity in CESM-H (Figure 8b, frequency ranges of 0.03 $\times 10^{-2}$ to 10^{-1} day^{-1}.) Current work is on implementing the spatially dependent diffusivity in high-resolution POP.

4.1.2. Atlantic Ocean

A common problem in global climate models is that the SST in the equatorial Atlantic is too warm in the East and too cold in the West, creating a zonal SST gradient of opposite sign to observed, notably between 50°W and 10°W [see, e.g., *Richter and Xie*, 2008, Figure 2; also *Toniazzo and Woolnough*, 2013, and references within these papers]. Most CMIP3 and CMIP5 models share these characteristics. A number of hypotheses have been proposed for why the models exhibit such features, including but not limited to effect of convection over land and effect on Equatorial winds [*Richter and Xie*, 2008], remote influence of southern

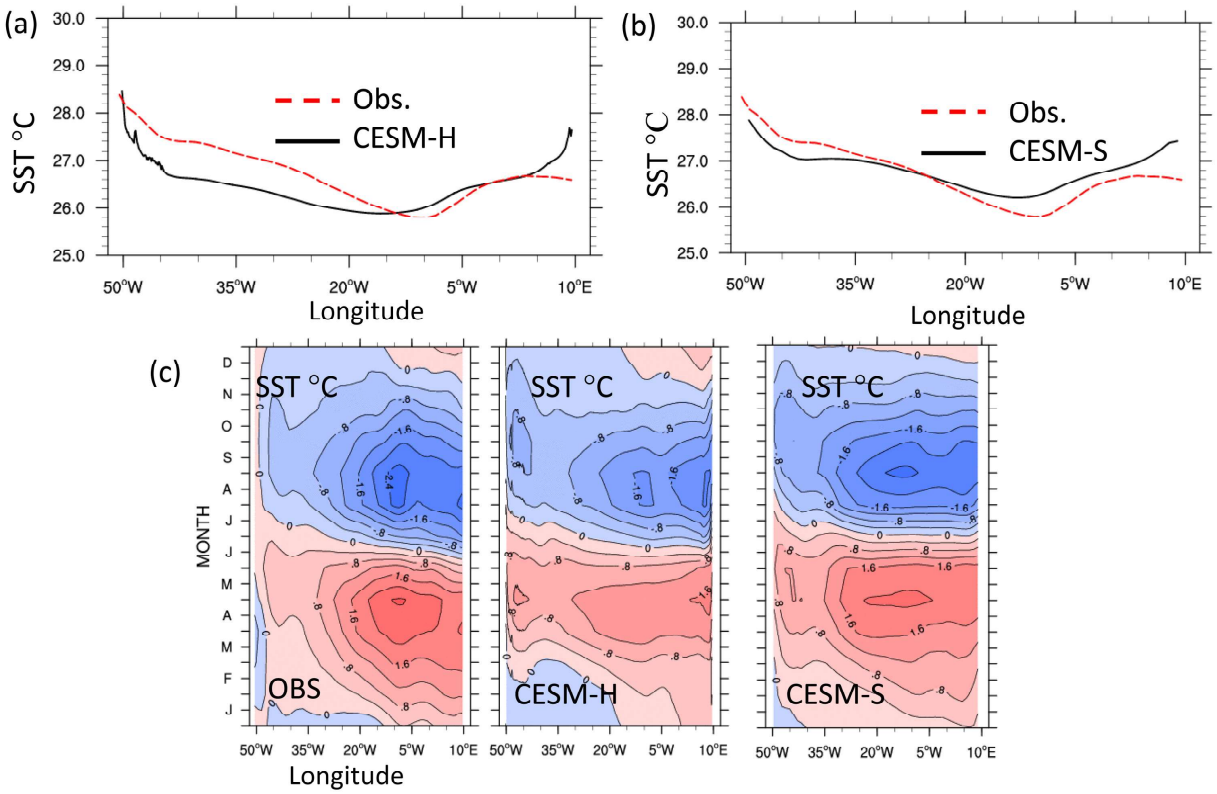

Figure 10. As Figure 7 but for the Atlantic Ocean.

stratocumulus (e.g., *Ma et al.* [1996] for the Peruvian case) [*Wahl et al.*, 2011], and remote influence of coastal upwelling [*Large and Danabasoglu*, 2006].

An encouraging aspect of CESM-S and CESM-H is that the zonal SST gradient between 50°W and 10°W is of the right sign but weaker than observed (Figure 10a). The gradient in CESM-S is slightly closer to observations (Figure 10b) and in general the CESM-S SST is warmer than CESM-H (Figure 10a). Both simulations are too warm by up to 1°C at the eastern boundary. In addition, the phase of the annual cycle is faithfully reproduced in both experiments (Figure 10c), but with slightly weaker amplitude in CESM-H. Overall, the results are quite impressive compared to CMIP3 and CMIP5 class models [e.g., *Richter and Xie*, 2008].

The key seasonal transition in the equatorial Atlantic is between March-April-May (MAM), when a warm pool exists in the Tropical Atlantic in observations and the model simulations, and JJA, when the cold tongue develops (Figure 11a) and the African monsoon gets under way. This is also the period when CCSM4 model biases grow largest [*Grodsky et al.*, 2012]. By JJA, the cold tongue is prominent in observations (Figure 11a), and is also clear in CESM-S (Figure 11b) and CESM-H (Figure 11c), albeit at a slightly warmer temperature (by about 1°C). During MAM, the observed winds in the equatorial zone are south-easterly on and south of the Equator (Figure 11d). Previous models such as CCSM4 have winds that are very weak along the Equator with a westerly bias [*Grodsky et al.*, 2012; *Muñoz et al.*, 2012]. In contrast, CESM-S (Figure 11e) and particularly CESM-H (Figure 11f) reasonably reproduce the magnitude of south-easterly winds, which would cause Equatorial upwelling [*Philander and Pacanowski*, 1981] and the development of a cold tongue.

One of the factors that influence the equatorial Atlantic winds is the precipitation over the Amazon rainforest, which has been found to be generally too weak in MAM in climate models [*Chang et al.*, 2007; *Richter and Xie*, 2008]. In addition, *Seo et al.* [2008] suggest that increased precipitation in the Atlantic ITCZ associated with more active convergence in easterly waves in high-resolution atmosphere models can improve the winds along the equator. CESM-H does have more precipitation in this season over most of Amazonia

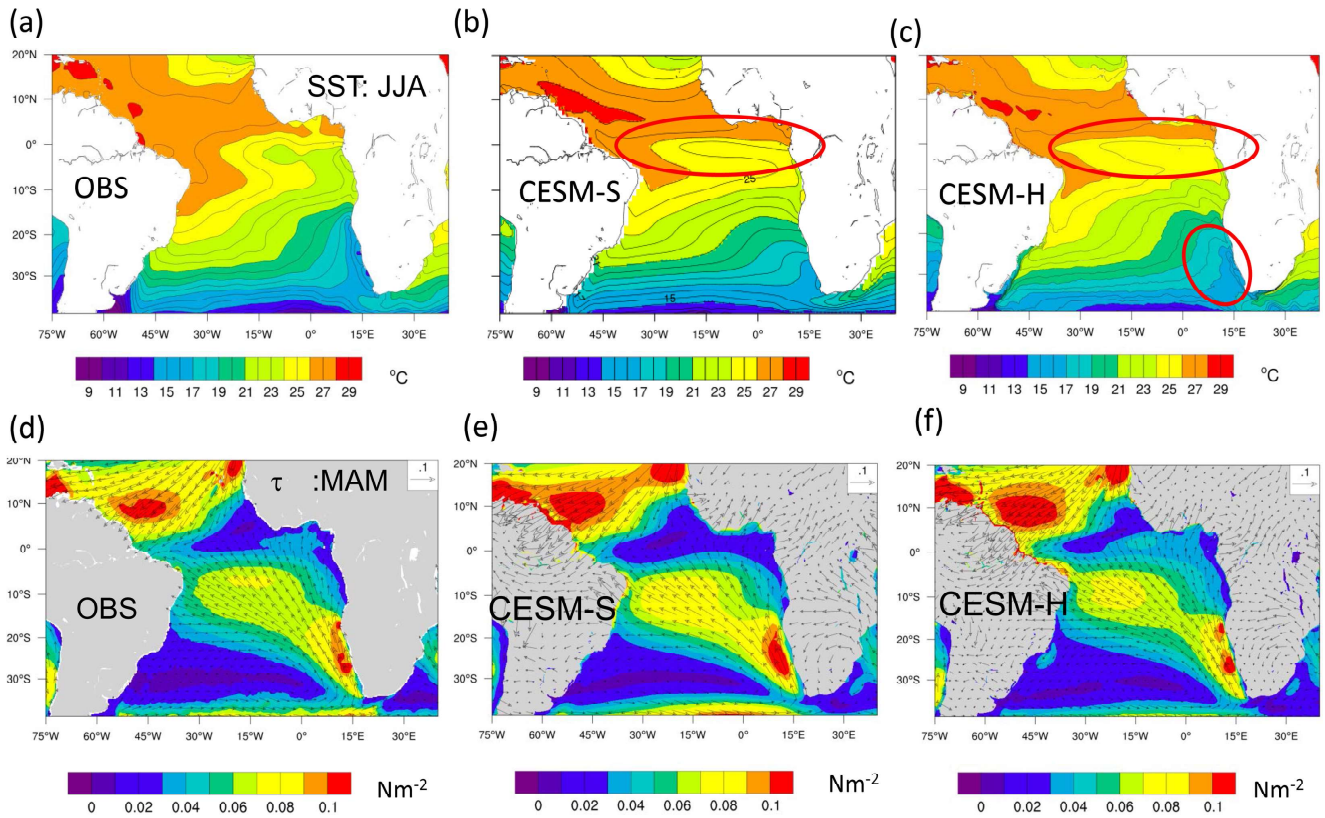

Figure 11. Climatological Mean SST for June-July-August (JJA): from (a) Levitus/WOA98, (b) CESM-S, and (c) CESM-H. Corresponding climatological mean wind stress vectors (Nm^{-2}) and magnitude of the mean vectors (color) in March-April-May (MAM) from (d) QuikSCAT observations [*Risien and Chelton*, 2008], (e) CESM-S, and (f) CESM-H.

and less over the Andes, compared to CESM-S, as found in the experiments of *Delworth et al*. [2012], although the CESM-H precipitation is larger than the TRMM estimate (Figure S1). More research is required to fully understand the nature of SST differences between CESM-H and CESM-S, the improvements since CCSM4, and the role of land convection versus the ITCZ over the ocean, which is also much stronger in CESM-H as noted in section 3.2.

A larger contrast between CESM-S and CESM-H is seen in terms of the SST in the Benguela upwelling region (circled in Figure 11c). Whereas the CESM-S (Figure 11b) SST field looks similar to CCSM4 (with ocean and atmosphere at 1°) in this region (not shown), with no indication of upwelling and a large warm bias in the model, the CESM-H (Figure 11c) does have more realistic SST. At first sight, this is encouraging, but a more detailed investigation (see Figure S2) has shown that although the CESM-H winds compare very well with observations in this region (Figures 11d and 11f), there is an overstrong wind stress curl near the coast, due to the gradient between strong wind stress in the atmospheric jet and weak wind stress at cells immediately adjacent to the coast. The latter, in turn, is due to the incorporation of atmosphere states over land in the regridding to coastal ocean cells, where values of wind over land are typically much weaker than over ocean due to increased surface drag (see *Kara et al*. [2007], for discussion of this issue). The end result is quite strong upwelling just offshore due to excessive Ekman pumping (Figure S2), but a not very realistic surface current and coastal upwelling field due to the lack of strong wind stress adjacent to the coast.

4.2. El-Niño Southern Oscillation (ENSO)

ENSO in the high-resolution model exhibits much more realistic amplitude and spectral characteristics than state-of-the-art nominal resolution climate models. The standard deviation of the Nino34 index is 0.68°C in CESM-H (years 15–85) which compares well with observations (0.73°C from 1935 to 1995), and represents a significant improvement with respect to CESM-S (1.21°C, years 15–150). Noting that ENSO exhibits strong

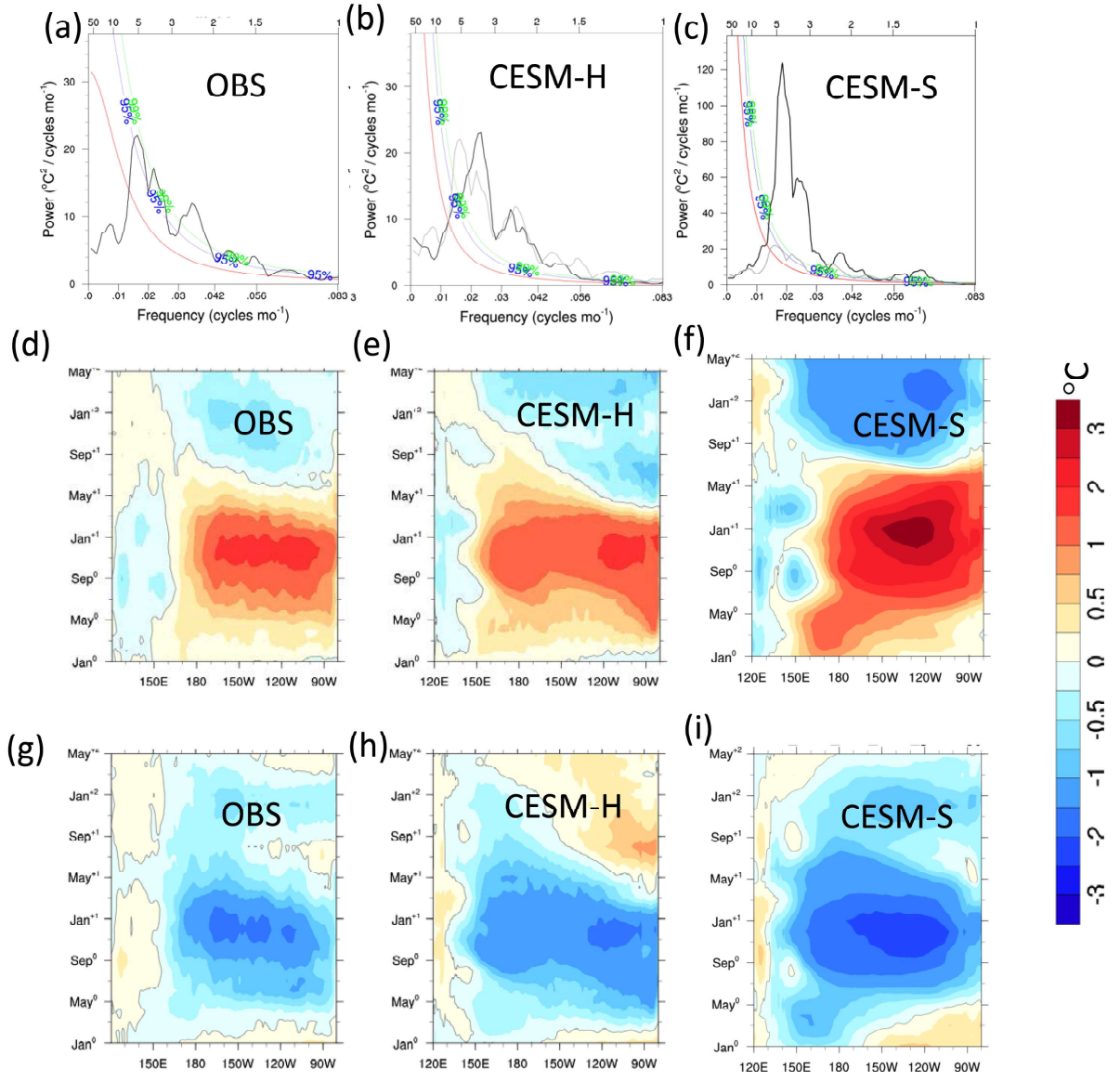

Figure 12. Power spectrum of Nino3.4 index from (a) the last 90 years of HadISST observations, (b) CESM-H, and (c) CESM-S. The 95% significance levels are overlaid. In Figures 12b and 12c, the HadISST spectrum is overlaid as thin gray line. Note change of ordinate range between Figures 12b and 12c. Composite El-Niño evolution shown as SST between 3°S and 3°N as function of calendar month for (d) HadISST observations, (e) CESM-H, and (f) CESM-S. (g–i) As Figures 12d–12f but for La-Niña.

multidecadal to centennial modulation of ENSO's amplitude [*Wittenberg*, 2009], our simulation may be too short to robustly estimate the amplitude of ENSO. However, when we compare the running 30 year standard deviation of the above runs with long control runs of CESM (with CAM5 Finite Volume atmosphere) and CCSM4, we find that periods of similar low standard deviation to CESM-H last for no more than 50–60 years in the long CESM simulation, and never occur in CCSM4, suggesting that indeed CESM-H robustly simulates a weaker ENSO (see Figure S3).

Further, the power spectrum of the Nino3.4 index simulated by CESM-H has a similar shape and magnitude to HadISST observations (Figures 12a and 12b). This represents a notable improvement with respect to previous versions of CESM and state-of-the-art climate models. For example, in CCSM3, the repeat period of ENSO was too regular (~2 years), whilst in CCSM4, the power spectrum was broader, as seen in observations, resulting from changes to the deep convection scheme [*Neale et al.*, 2008; *Gent et al.*, 2011], but the

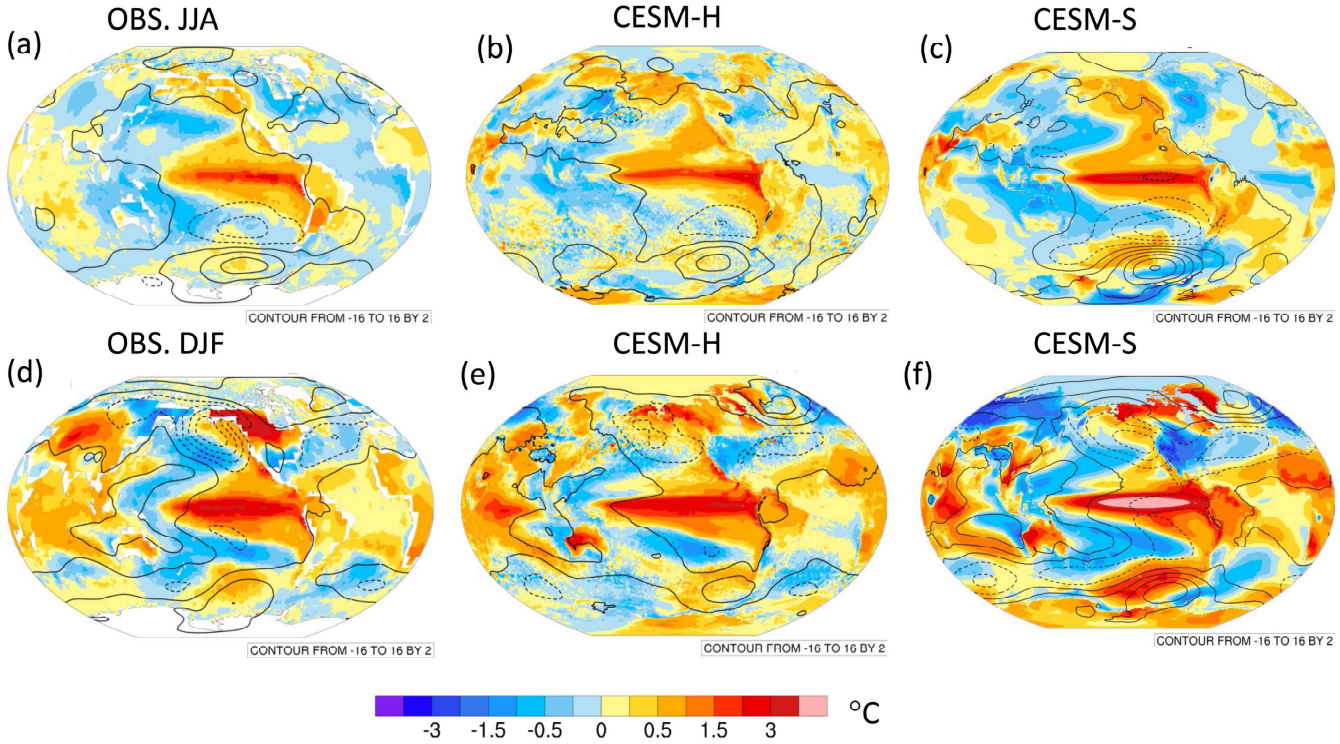

Figure 13. ENSO composites based on warm minus cold events of greater than ±1 standard deviation of Nino3.4 time series. (a–c) For JJA before the peak and (d–f) for following DJF. Years 1920–2011 of HadISST and NOAA Merged Land-Ocean Surface Temperature Analysis (MLOST) [*Smith and Reynolds*, 2005] land surface temperature, and sea level pressure (SLP) from the twentieth Century Reanalysis [*Compo et al*., 2011] (Figures 13a and 13d). CESM-H years 15–100 (Figures 13b and 13e), and CESM-S, years 1–166 (Figures 13c and 13f). Surface temperature (°C, color) and SLP (contours—interval 2hPa).

variance of the Nino3.4 index was much too high. This has persisted into some recent versions of CESM1 with the CAM5 model.

The Nino34 spectrum exhibits two notable peaks: at around 5 years and a smaller peak at 2.5 years in observations (Figure 12a, black line, and Figures 12b and 12c, gray lines): and at 3.5 years and again at 2.5 years in CESM-H (Figure 12b, black line), the longer period peaks having power around 20°C^2/cycles/month in both cases. In contrast, CESM-S has a much stronger and more regular power spectrum with an excessively strong peak of 120°C^2/cycles/month (Figure 12c, note change of ordinate range). This seems to be unusually strong even by CCSM4/CESM standards, but the previous long control runs of CCSM4, and of CESM, also had more power than the high-resolution model, both having single, broad peaks reaching nearly 70°C^2/cycles/month and 40°C^2/cycles/month, respectively.

In addition to the power spectrum, another important aspect is how the El-Niño and La-Niña events develop. Composite Hovmoller plots of El-Niño show reasonable timing in CESM-H (Figure 12e) compared to observations (Figure 12d). The CESM-S El-Niño is too strong too early in the west-central Pacific (Figure 12f). However, composite La-Niñas show that CESM-H (Figure 12h) does not capture the observed recurrence of la-Niña in the second year (see Figure 12g). This contrasts with CESM-S (Figure 12i) and the previously mentioned long CCSM4 and CESM1 control runs, which *do* exhibit the second-year La-Niña [see *Deser et al*., 2012]. (Note that for CESM-H there were 14 El-Niño and 13 La-Niñas used for the respective composites, whilst for CESM-S 26 El-Niño and 30 La-Niñas were used, for both Figures 12 and 13.)

The spatial SST and sea level pressure distribution during ENSO events is displayed as a composite of warm minus cold events for observations (Figures 13a and 13d) CESM-H (Figures 13b and 13d), and CESM-S (Figures 13c and 13f). In June-July-August preceeding the peak (JJA^0), the basin-scale SST anomaly in the Pacific Ocean is well reproduced by the model at both resolutions, as are the teleconnections to the south-east South Pacific ocean, seen as a cyclonic/anticyclonic couplet of surface pressure cells to the north/south respectively (Figures 13a−13c). However, as expected from Figure 12, the magnitude of these features is

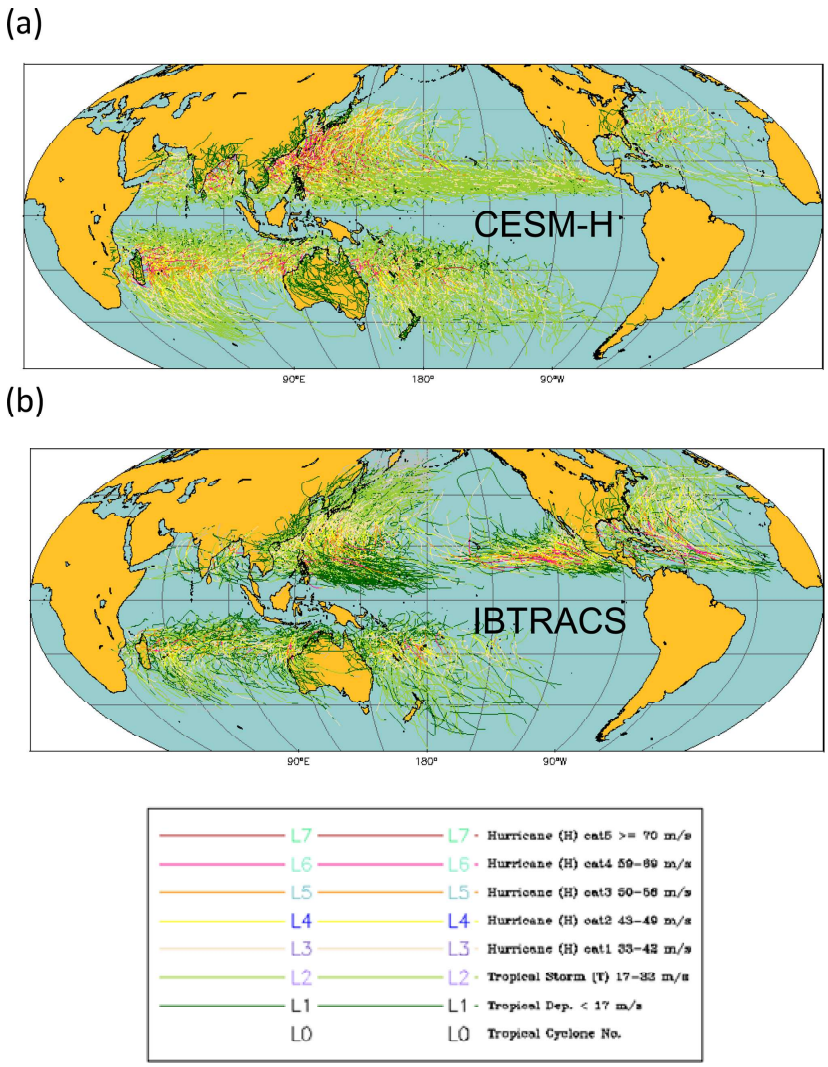

Figure 14. Tropical cyclone and hurricane tracks: (a) from a 30 year segment (years 60–90) of CESM-H and (b) from the IBTRACS analysis of observations for 1970–1999 (derived from *Knapp et al.* [2010]). Storms with maximum wind speed > 33m/s shown. The tracking method is described in *Bacmeister et al.* [2014].

stronger in CESM-S than observed, whilst CESM-H is more comparable with observations. In JJA preceeding the peak and through to the peak period of December-January-February (DJF), CESM-H has a maximum SST signal in the far-east equatorial Pacific (classic El-Niño, Figures 13b and 13e) whereas observations (Figures 13a and 13d) and CESM-S (Figures 13c and 13f) maximize further west, suggesting an influence of central Pacific/Modoki El-Niño. Finally, the low pressure cell over the north-east Pacific in DJF, part of the "atmospheric bridge" which acts to cool N. Pacific SST [*Alexander et al.*, 2002], is weaker in CESM-H (Figure 13e) and in CESM-S (Figure 13f) than in observations (Figure 13d), more so in CESM-H. Put another way, the N. Pacific teleconnection is weak even when the equatorial Pacific SST signal is too strong (Figure 13f), and it gets weaker still when the equatorial SST signal gets weaker (Figure 13e). Note however that there can be considerable model variability of N. Pacific response in multidecade means, as indicated by *Alexander et al.* [2002], for ensembles of 50 year integrations (see their Figure 14).

4.3. Intraseasonal and Synoptic Variability

4.3.1. Tropical Cyclones

Comparison of the CESM-H Tropical Cyclone (TC) tracks with the observed record [International Best Track Archive for Climate Stewardship (IBTRACS); *Knapp et al.*, 2010] reveals that the model has too little TC

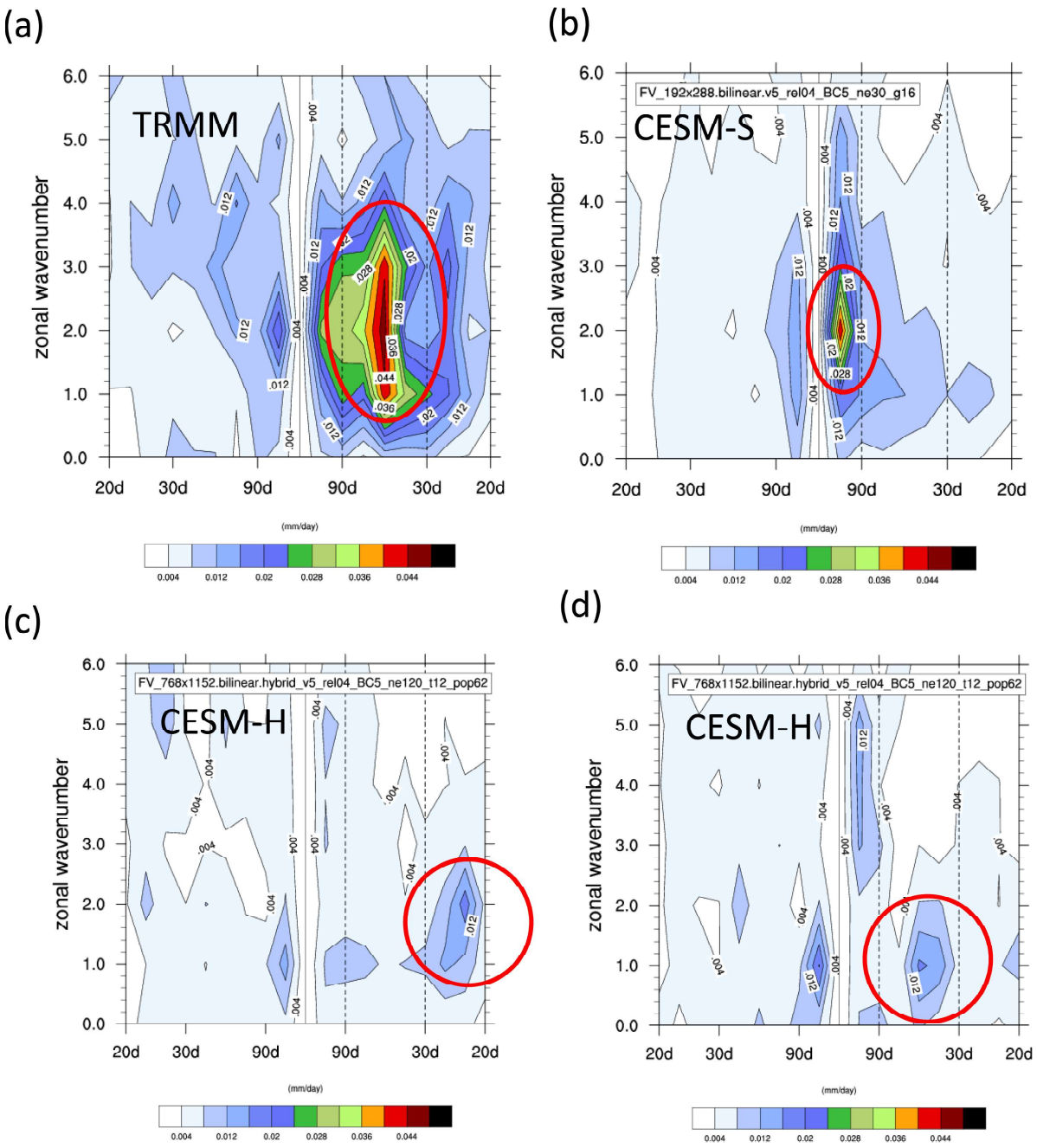

Figure 15. Wavenumber (ordinate)-frequency (absicca) spectrum of tropical precipitation variability in DJF. (a) TRMM, years 2000–2010, (b) CESM-S, years 136–167. (c) CESM-H, years 64–74, (d) CESM-H years 75–85. Circled regions are referred to in the text.

activity in the North Atlantic and eastern Pacific, but too much strong hurricane (Category 3–5) activity in the West Pacific, and Bay of Bengal (Figure 14). The former is a common problem amongst climate model that permit TCs, and may relate to below-observed SST in the former regions and above-observed SST in the latter (Figure 3a), but other factors such as wind shear and tropospheric temperature difference may have an influence. A 0.25° atmosphere-only simulation with observed HadISST surface boundary conditions and with similar model configuration of CAM5 to our run does exhibit more realistic North Atlantic and East Pacific TCs, suggesting SST is an important factor, but it also exhibits perhaps overactive TC activity in the

West Pacific (A. Gettelman, personal communication, 2013). Another notable feature of CESM-H is that it does not have the minimum in TC activity observed in the north central Pacific near the dateline, suggested by *Bacmeister et al.* [2014] to relate to ITCZ biases. Note that only climate models of resolution of around 0.5° or finer exhibit active TCs so an advantage of the CESM-H run (and previous long high-resolution runs mentioned in the Introduction) is that large-scale and long period climate modes can be analyzed together with their influence on TCs (such as Atlantic MultiDecadal Variability and ENSO).

4.3.2. Intraseasonal Variability

Observed intraseasonal tropical precipitation variability is dominated by the eastward propagating Madden-Julian Oscillation, as shown in wavenumber-frequency spectra of TRMM precipitation measurements in winter (Figure 15a, red circle, and the dashed vertical lines demark the intraseasonal range between 30 and 90 days). CESM-S has energy at longer periods (Figure 15b), a common feature of CAM5 and CESM at this resolution. The CESM-H run exhibits considerable decade to decade differences in the intraseasonal variability: some decades have negligible intraseasonal variability but a suggestion of shorter period variability (Figure 15c), whilst other decades do have variability at a frequency similar to observations but with weaker amplitude than observed and a narrower wavenumber range (Figure 15d). As with many previous climate model simulations, the ratio of energy in eastward versus westward propagating features is much smaller than observed. It can also be seen that in some cases, there is an improvement in propagation characteristics of the dynamical intraseasonal variability (e.g., in zonal wind at 850 hPa) in CESM-H relative to CESM-S and uncoupled CAM5, but the precipitation signals remain fairly weak (Figure S4).

5. Midlatitude Atmosphere and Ocean Synoptic Variability

In the midlatitudes, small-scale features of importance include (but are not limited to) orographically forced precipitation, ocean eddies and their interaction with the atmosphere, storm tracks, and cold air outbreaks. High resolution has been suggested to improve simulation of these features, by better resolving orography [*Delworth et al.*, 2012], ocean fronts and eddies (e.g., Western Boundary Currents [*Bryan et al.*, 2007]), and their interaction with the atmosphere storm track [*Small et al.*, 2014, and references therein]. These processes are described here with reference to the new CESM simulations.

5.1. Mesoscale Convective Systems off the Rockies

Over the continental U.S. during the warm season, there is a late afternoon local precipitation maximum over the Rockies (between 100°W and 105°W) which leads to a nocturnal precipitation maximum over the Plains (near 98°W–95°W) through the eastward propagation of precipitation, as documented originally in surface rain gauge data, and high-resolution radar data [e.g., *Wallace*, 1975; *Carbone et al.*, 2002], and more recently in satellite data. Observations show that during the warm season, in the continental interior to the lee of topography, much of the precipitation can be attributed to mesoscale convective systems (MCSs) [*Laing and Fritsch*, 1997]. Typically, these MCSs and their eastward propagation in the lee of mountains are not simulated by GCMs due to the models' coarse resolution and limitations of parameterized convection schemes [*Pritchard et al.*, 2011].

A time-longitude diagram of the observed precipitation shows the timing of the diurnal signature over the Rockies (Figure 16a) with a maximum at about 00Z near 102°W, and an associated eastward propagation of the precipitation maximum to between 90°W and 95°W by 12Z. In CESM-H run (Figure 16b), we also see propagating features (circled) with a diurnal precipitation maximum over the Rockies at about 102°W at 00Z and eastward propagation to just east of 100°W by 06Z. In addition, a feature is seen at 105°W at 00Z, which is almost stationary until 006Z, as well as a secondary maximum just west of 95°W at 09Z. A case study of the progression of a precipitation event and its eastward propagation is illustrated in Figure S5, and the location of an animation of such an event is given in the Acknowledgments.

The MCS events in CESM-H occur in April and May (in the only year of hourly data from the run), while in observations they are more robust and coherent in June and July. Observed MCS over the Rockies exhibit considerable interannual variability [*Carbone et al.*, 2002], and it may be the case that the one model year is not representative of a longer-term average. Further, the modeled propagation speed (about 5–10 m s^{-1}) is slow compared to the observed composite ($\sim$16 m s^{-1}), but observations show a broad range of propagation speeds varying from 7 to 30 m s^{-1} in individual events. Further investigation of the characteristics of

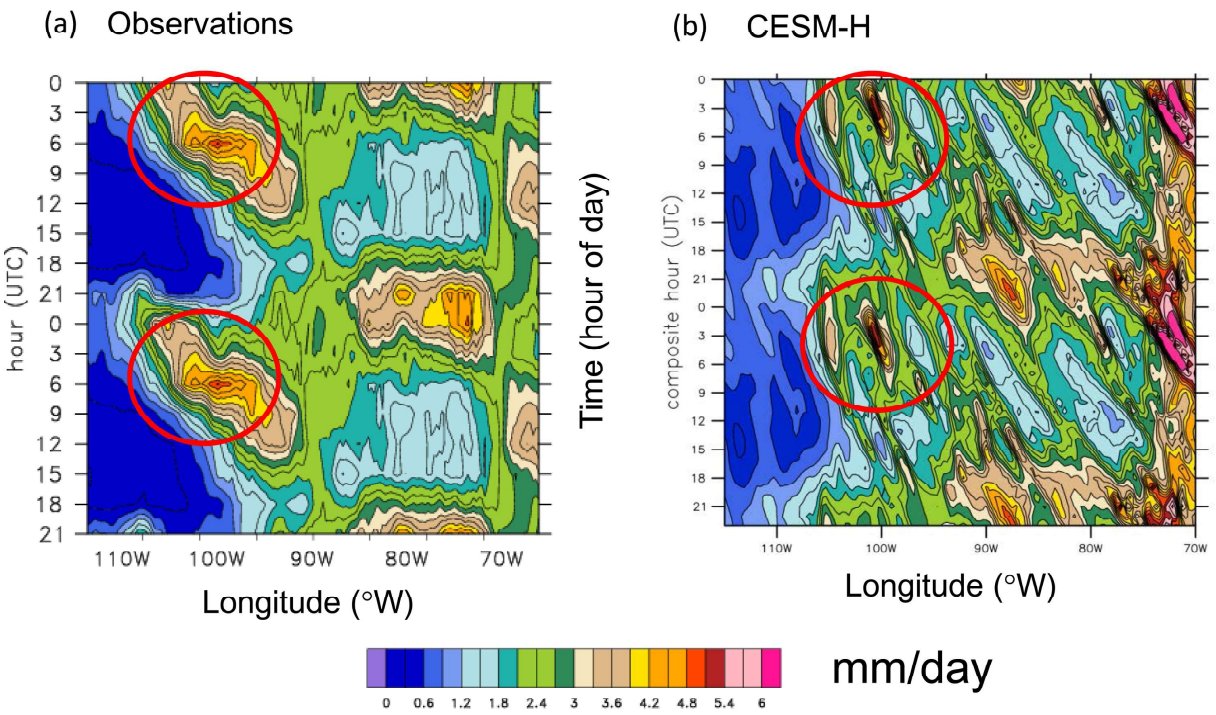

Figure 16. Diurnal cycle and propagation of precipitation over Rockies. The composite time (in local hours) versus longitude diagram for precipitation from (a) TRMM observations averaged over June and July and (b) one season (April to May) of CESM-H with available hourly data.

the model events compared with observations and other resolution simulations (including atmosphere only at 0.125°) is planned.

5.2. Extratropical Storm Tracks Including Cold-Air Outbreaks and Ocean Fronts

Field campaigns such as KESS [*Donohue et al.*, 2008] and CLIMODE [*The Climode Group et al.*, 2009] have identified strong air-sea interaction at western boundary currents [see reviews by *Kelly et al.*, 2010; *Kwon et al.*, 2010]. Notable features are the cold-air outbreaks that occur over the western North Atlantic and North Pacific, when large sensible and latent heat fluxes occur as cool continental air flows over the relatively warm ocean waters. Depending on the season, the upward heat fluxes may occur in the coastal zone (usually in deep winter, when coastal water is warmer than continental air), or over the warm western boundary currents, Gulf Stream and Kuroshio Extension (often in spring, when SST at the coast is colder than the near-surface air temperature, which in turn is colder than the SST in the western boundary current) [*Young and Sikora*, 2003]. These upward heat fluxes can fuel synoptic atmospheric storms and provide a link between the surface and the free troposphere [*Booth et al.*, 2012, and references therein]. Examples of individual cold air outbreaks in CESM-H are shown in Figure S6 and the location of an animation of 1 years worth of hourly data showing global latent heat flux over SST is given in the Acknowledgments.

Here we investigate the net effect on the climatological mean latent heat flux. For comparison, we use a high-resolution (0.25°) version of the Objectively Analysed air-sea FLUX data set (OAFLUX) [*Yu and Weller*, 2007], which has been described and assessed in *Jin and Yu* [2013] and is referred to as OAFLUX-0.25°.

The wintertime (DJF) mean of latent heat flux (LHFLX) from OAFLUX-0.25° shows maximum along the Gulf Stream core of warm water of just over 350 W m^{-2} (Figure 17a). There are two notable differences about the corresponding CESM-H field (Figure 17b): first, the band of maximum LHFLX separates from the continent further north than observed, and second, the maximum values are much higher, up to 475 W m^{-2} in the core of the Gulf Stream. The first difference may reasonably be assumed to be due to the too-northward separation of the Gulf Stream warm water core (see Figure 17d). Insight into the second difference is found by examining the climatological LHFLX from the uncoupled CESM-A simulation

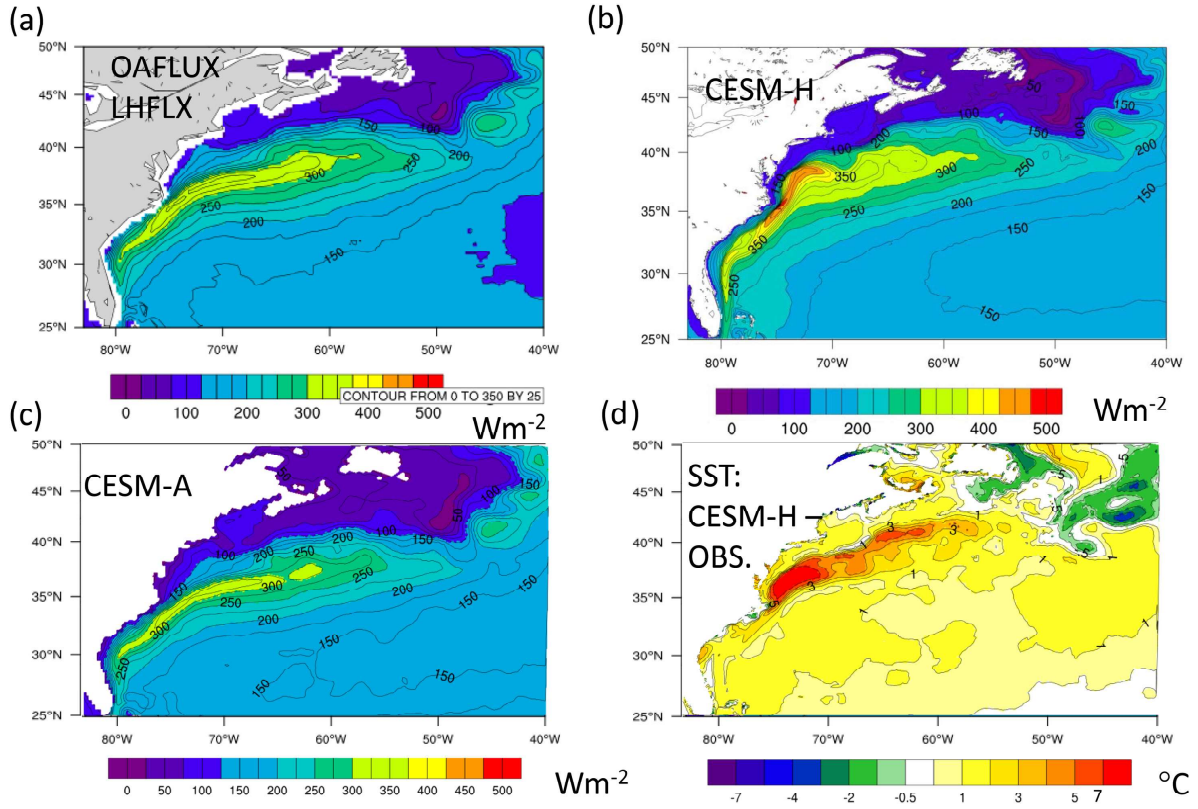

Figure 17. Climatological mean for DJF of latent heat flux from (a) OAFLUX-0.25°, (b) CESM-H, and (c) CESM-A. (d) Corresponding SST difference between CESM-H and OISST-0.25° [*Reynolds et al.*, 2007]. (The latter was used as surface boundary condition for CESM-A.) Figures 17c and 17d cover the same geographic area as Figures 17a and 17b.

(Figure 17c)—this takes values much closer to OAFLUX-0.25° (Figure 17a) than CESM-H (Figure 17b). As the atmosphere model is identical in CESM-H and CESM-A, this suggests that the higher LHFLX in CESM-H is due to SST errors rather than internal atmospheric dynamics and upstream states (e.g., winds, low level humidity).

The SST in CESM-H is too warm by over 7°C in the Gulf Stream "overshoot" region (i.e., where the Gulf Stream erroneously enters the region of observed, much colder, shelf waters giving rise to the bull's-eye of SST difference), and there is a broader warm anomaly of between 1°C and 2°C in the subtropical north-west Atlantic (Figure 17d), part of the general extratropical warming noted with respect to Figure 3. The broad warmth of CESM-H compared to observed SST will lead to more surface instability and increase the LHFLX, as will the more nearshore path of the Gulf Stream after Cape Hatteras, because air coming off the continent will have less time to adjust to the underlying ocean before meeting the Gulf Stream.

Note that the LHFLX errors in CESM-S are more extensive than in CESM-H, due to the larger SST errors in the former case (Figure 3), and the broad cool SST difference east of the North Atlantic Current (Figure 3b) leads to LHFLX errors of ~ -100 W m^{-2} in that region (not shown).

It has also been noted in observations that the highest frequency of strong winds near the surface, and the highest synoptic surface wind variability, occurs on the warm side of ocean fronts [*Sampe and Xie*, 2007; *Joyce et al.*, 2009; *Booth et al.*, 2010]. Atmosphere models with relatively smooth SST do not show such localized maxima over the oceans [*Small et al.*, 2014] and current research is on whether coarse or fine resolution coupled models can capture the same features. Figure S7 shows that CESM-H has a slightly stronger and narrower peak of synoptic variability at 10 m over the Gulf Stream and downstream of the Kuroshio Extension in DJF (Figure S7a) than CESM-S (Figure S7b), while both are much stronger than corresponding fields from ERA-Interim reanalysis (Figure S7c). A full analysis of the surface storm track, its variability and relationship with the free tropospheric storm track is underway.

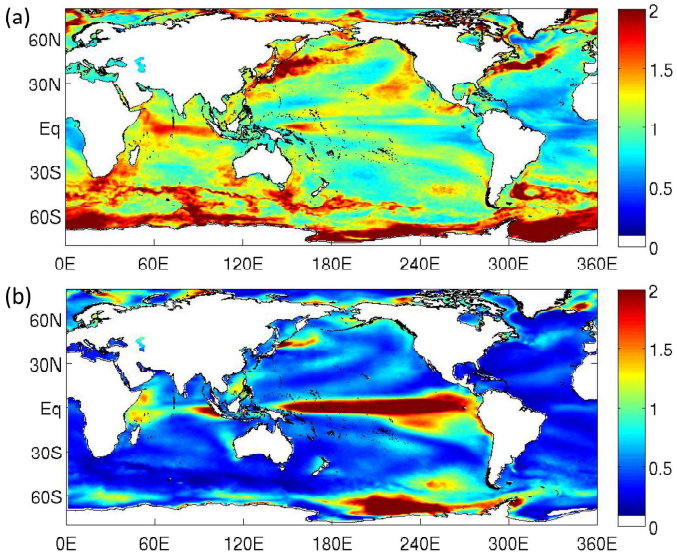

Figure 18. The ratio of the standard deviation of SST variability between model and OISST-0.25° [*Reynolds et al.*, 2007]. The annual cycle is removed from the monthly data. (a) CESM-H, years 60–90 and (b) CESM-S, years 136–165.

5.3. Ocean Variability

Ocean variability in the model, measured in terms of SST and Sea Surface Height (SSH), was compared against that seen in OISST-0.25° [*Reynolds et al.*, 2007] and in the weekly Archiving, Validation and Interpretation of Satellite Oceanographic (AVISO) merged product [*Ducet and Le-Traon*, 2001], respectively. The standard deviation of SST (hereafter σSST) in CESM-H captures the same spatial characteristics found in the NOAA OI, with high σSST in the western boundary current extensions and the Antarctic Circumpolar Current (ACC), but the magnitude of σSST in CESM-H is up to two times higher in the Gulf Stream, Kuroshio Extension, and ACC (Figure 18). The large ratios of variability are not mainly due to displacements of the regions of variability but represent an actual strengthening of variability in the model (Figure S8). There is an overall too-low σSST bias in the Tropical and North Atlantic which may be connected to the lack of Tropical cyclones in the Atlantic (Figure 14). The Tropical Pacific σSST is better represented in CESM-H than the Atlantic, but still slightly weak (Figures 18 and S8).

In the standard resolution CESM-S, σSST is very low in most regions of the Globe except for the equatorial Pacific and east Indian Ocean (related to ENSO variability discussed earlier), the west Tropical Indian Ocean, Kuroshio/Oyashio Extension, and the subpolar south-east Pacific (possibly related to the strong ENSO teleconnection). SST variability in the Kuroshio/Oyashio Extension in this resolution model has been discussed by *Thompson and Kwon* [2010], who found that the model places the oceanic jet in the region of highest SST gradient, so that fluctuations of the jet causes large SST anomalies. In contrast, observations show that the jet and the strongest SST gradient are displaced meridionally by almost 500 km and hence the SST variability is less.

The standard deviation of CESM-H sea surface height (hereafter σSSH, Figure 19b) compares well with the AVISO product, (Figure 19a). There is a less notable overestimation of σSSH than with σSST, but the western boundary currents (notably Kuroshio Extension, Brazil/Malvinas confluence) and ACC are still too strong. In the equatorial Pacific, by contrast, σSSH is too weak in CESM-H, as also seen in the SST (Figure 18). In CESM-S (Figure 19c), SSH variability is weaker than observed everywhere except in the Tropical Pacific and Indian Ocean. The larger variability of SSH in the eastern equatorial Pacific in CESM-S relative to CESM-H is consistent with the larger SST variability in the former (Figure 18), partly due in turn to the strong ENSO activity (Figure 12).

σSSH for AVISO and CESM-H was further decomposed into different time period bands of (i) less than 90 days denoting the mesoscale band (ii) 90–400 days the annual cycle and harmonics, and (iii) greater than 400 days for low frequency variability. σSSH in each of the different frequency bands compare quite well between the model and observations (Figure S9) except in the Kuroshio Extension, tropics, and Southern Ocean. The Kuroshio Extension has higher variance in the mesoscale band in the model (Figures S9a and S9b). More analysis of Kuroshio extension eddy variability, its heat transport, and relationship to atmosphere heat transport, can be found in [see also *Bishop and Bryan*, 2013; S. P. Bishop et al., Bjerknes-like compensation between eddy components of meridional heat transport in the wintertime North Pacific, submitted to *Journal of Physical Oceanography*, 2014]. In contrast to the Kuroshio Extension region, the equatorial Pacific

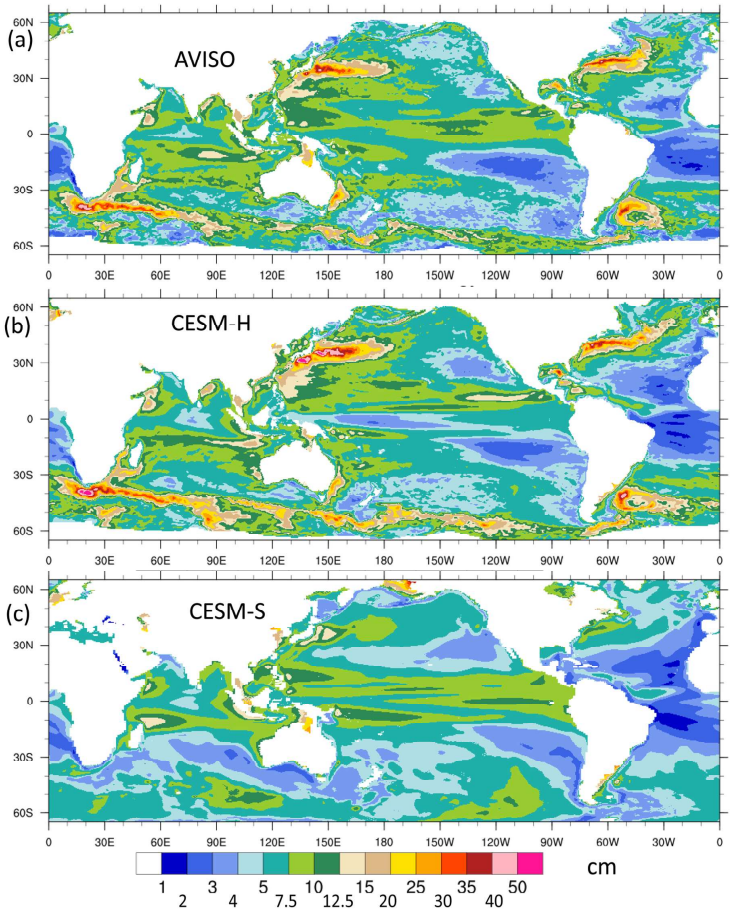

Figure 19. Standard deviation of sea surface height (SSH) variability (in cm) from (a) observations (AVISO), (b) CESM-H, and (c) CESM-S. Note nonlinear color scale. CESM-H data have been put on the AVISO grid.

has too low σSSH at low frequencies in CESM-H (Figures S9c and S9d). Thus, despite the impressive SST power spectrum (Figure 12) in Nino3.4, the high-resolution model has a weak SSH variability. In the Southern Ocean ACC, σSSH is high in CESM-H across all the frequency bands (Figure S9).

6. Discussion

A question that arises from the current study is why the new generation CESM model avoided the initial and sizeable surface trends seen in previous high-resolution CCSM4 simulations (overly thick Arctic ice and cool high northern latitude SST in *McClean et al.* [2011], and a dramatic reduction of Arctic sea ice and generally overwarm temperatures in *Kirtman et al.* [2012]. *McClean et al.* [2011] point to an intensified and contracted polar vortex helping to produce the high-latitude Northern Hemisphere cold state, via increased surface wind stress. *Kirtman et al.* [2012] suggest that too much ocean heat transport contributes to the Arctic warming, leading to a reduction in Arctic sea ice, which triggered ice-albedo feedbacks to further warm the high latitudes.

The ocean meridional heat transport from CESM-H and the Kirtman et al. simulation is shown in Figure 20. Overall, the total heat transport is similar between the two cases, but there is slightly more total heat transport in the Tropical Northern Hemisphere peak, and slightly less in the subpolar gyre, in CESM-H. Weaker heat transport in the subpolar gyre is one possible factor for more sea-ice in the CESM-H than in *Kirtman et al.* [2012].

In the Northern Hemisphere *winter*, the current high-resolution simulation shows some evidence for the strong and contracted polar vortex seen in *McClean et al.* [2011] (but it is much less pronounced in the *annual mean* in our simulation). Hence the wind stress in mid and high latitudes in this new run in winter is just as strong as that seen in the *McClean et al.* [2011] simulation. (Compare Figures 5a and 5b of current

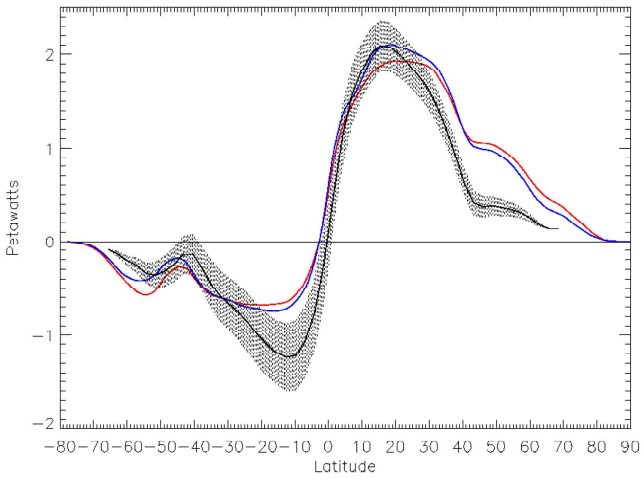

Figure 20. Total global northward ocean heat transport, from years 35–60 of CESM-H (blue curve) and from the high-resolution CCSM3.5 simulation of *Kirtman et al.* [2012] (red curve). The mean (black line) and estimated range (shaded) derived from observations is from *Trenberth and Caron* [2001].

paper with Figure 5 of *McClean et al.* [2011], and note that differences in the climatological mean wind stress vectors between QuiKSCAT and ERS-scatterometer are much smaller than the model-observation differences.) The first 15 years or so of our new simulation did show global ocean cooling (see Figure 2a near the ocean surface) as the model adjusted to the initial conditions. However, there was no evidence of the large >5°C cooling of the N. Atlantic subpolar gyre, nor of the rapid Arctic sea ice growth seen in *McClean et al.* [2011].

Our CESM-H experiment also exhibits key improvements in the simulation of ENSO. El-Niño and La-Niña events are much weaker in CESM-H, in closer agreement with observations. Myriad processes govern the amplitude of ENSO, complicating the attribution of this improvement. The strength of the feedbacks involved in the growth and decay of ENSO events is controlled by the mean and seasonal climate of the equatorial Pacific, including the zonal SST gradient, the thermocline depth and stratification, as well as the strength of the equatorial trade winds [*Fedorov and Philander*, 2001; *Meehl et al.*, 2001; *Jin et al.*, 1994]. Atmospheric processes, such as the response of deep convection and air-sea fluxes to SST anomalies, could play an equally important role [*Guilyardi et al.*, 2006; *Bellenger et al.*, 2014]. Therefore, attributing the cause of improved ENSO simulation is not straightforward.

Stronger stratification, shallower thermocline, or zonal wind stress in the western equatorial Pacific can lead to stronger ENSO [*Meehl et al.*, 2001]. Conversely, stronger easterlies east of the dateline are associated with weaker ENSO variability [*Kirtman and Schopf*, 1998; *Burgman et al.*, 2008]. However, differences in these features of the mean climate among the experiments and observations do not directly explain why CESM-H simulates weaker ENSO than CESM-S in better agreement with observations. The following are examples:

1. Both CESM-H and CESM-S simulate a deeper thermocline than observed, which would lead to a weaker El-Niño than observed. CESM-H has a deeper thermocline than CESM-S (e.g., 20°C isotherm at 150°W is at 150 and 135 m, respectively) but has a slightly stronger temperature gradient (going from 16°C to 22°C over 55 and 60 m, respectively, at the same longitude).
2. Meanwhile, the zonal SST gradient in CESM-H very well matches observations, and is stronger than CESM-S (compare Figures 7a and 7b), which should lead to a stronger Nino3.4 SST variability in the higher-resolution case.
3. Finally, Figures 5b and 5c shows that CESM-H has stronger than observed, and stronger than CESM-S, zonal winds in the east equatorial Pacific, which would suggests a reduction in ENSO variability following *Kirtman and Schopf* [1998].

In summary, the deeper thermocline of the high-resolution run, and stronger eastern Equatorial trade winds, are possible factors for the weaker Nino3.4 variability than in the standard resolution case, but further research is needed to confirm this, and determine the role of other ocean and atmosphere processes which would potentially control the amplitude and frequency of ENSO events.

Meanwhile, in the Tropical Atlantic, the present experiment appears to be the first high-resolution global model to simulate a reasonable cold tongue and location of the ITCZ. All of the previous high-resolution model studies show the well-known warm SST and southern ITCZ biases seen in lower-resolution runs. A key factor in the current model performance is the improvement of Equatorial winds, possibly related to

land convection over South America. We are currently investigating how much of this is due to the new physics schemes in CAM5, and how much due to resolution.

The use of high resolution in climate models enables the possibility of capturing small but possibly intense events, such as Tropical Cyclones, MCS, frontal-scale air-sea interactions. However, high resolution often comes at a price—many well-founded model schemes and parameterizations are designed for the coarser, more typical resolution models. As an example, excessive precipitation in the ITCZ is a common feature of high-resolution CAM5 and its predecessor CAM4 [*Bacmeister et al*., 2014], and is related to excessive low-level moist heating and the coupling of low-level convergence and precipitation [*Bacmeister et al*., 2014, D. Williamson, personal communication, 2013]. This and other reasons have led to the current development of new convection schemes for CAM, as well as research into scale-aware parameterization.

The occurrence of deep ocean warming in CESM-H is not unusual among global high-resolution climate models. Warming between 500 and 1000 m of comparable amplitude to our simulation was also seen by *Delworth et al*. [2012] in the CM2.5 model (0.5° atmosphere, 0.25° ocean). They found a much reduced subsurface drift in their CM2.6 simulation (0.5° atmosphere, 0.1° ocean) and attributed the large drift in CM2.5 to inadequate representation of eddies in the "eddy-permitting" regime, believing that the CM2.6 simulation corrected this by resolving eddies explicitly. Recently, *Griffies et al*. [2014] diagnosed the heat budget of this suite of simulations and concluded that CM2.6 better represents eddy transport of heat upward to counteract downward transport of heat by the mean flow, leading to a more balanced budget and reduced heating tendency in the top 1000 m of the ocean. Our results show slightly less warming in the 500—1000 m depth range in CESM-H compared to CESM-S, but more warming in the upper 200 m (especially in the first 30 years, Figures 2a and 2b). A parameterization of submesoscale processes [*Fox-Kemper et al*., 2008], which Griffies et al. (manuscript in preparation, 2014) show to be important in cooling the depths between about 50 and 500 m, has been included in CESM-S but not in CESM-H. Another factor is that our runs, like *Delworth et al*. [2012], used very short (1 year) ocean-ice spin-ups: *Sakamoto et al*. [2012] used a much longer (100 year) spin-up and achieved much smaller drift (∼0.1°C over 100 years) in their coupled simulation.

It may be argued that for the high horizontal resolution experiments discussed here, an accompanying increase in vertical resolution should have been applied [*Lindzen and Fox-Rabinovitz*, 1989]. Although experiments with a higher number of vertical levels in the free troposphere have recently been performed (giving a total of 60 levels [*Richter et al*., 2014]), they did not increase resolution in the boundary layer. Current and future work is on investigating the air-sea interaction response, and the mean climate, of simulations with extra vertical levels in boundary layer and higher (S. Park et al., personal communication, 2013).

The extensive and long data set generated under this study will hopefully be valuable to the community with interest in how increased resolution changes the mean and variability of the simulated climate. To this end, the data are available to the public, as described in the Acknowledgments below.

7. Summary and Future Plans

A new high-resolution CESM simulation has been performed for 100 years, the longest such simulation with CAM5. The main highlights of the run are as follows:

1. Equatorial Pacific SST biases are small (mostly $<0.2°$C), and globally the SST bias relative to observations is quite low compared to a standard resolution case.
2. The power spectrum of Niño3.4 SST time series reveals that the frequency and amplitude of ENSO is comparable to observations, with much less variance than previous CESM/CCSM runs. The typical generation and decay of El-Niño events compares well with the observed record, but the La-Niña events do not show the observed second-year reemergence.
3. There is a notably small SST bias in the equatorial Atlantic where a realistic cold tongue in the eastern basin develops in JJA and the ITCZ keeps mostly north of the Equator. Most climate models (including the CMIP5 generation and CCSM4) have a weak cold tongue or even a reversal of the zonal SST gradient. In this case, much of the improvement is also seen in the lower-resolution version of the model indicating a fundamental change from CCSM4 to CESM.

4. In the ocean, the model eddy field is very rich and comparable to observations in terms of SSH variability: however the SST variability is too high. Ocean fronts are quite well represented: long-standing issues of the Gulf Stream path overshooting at Cape Hatteras and being too zonal in its extension still exist, but the consequent SST biases are considerably reduced compared to standard resolution models.
5. A consequence of having strong SST gradients is that the overlying atmospheric boundary layer and storm track is modified, such that some of the strongest near-surface wind variability in the Globe occurs over the warm side of ocean fronts. In addition, huge amounts of heat are passed from ocean to atmosphere as cold winter continental air passes over western boundary currents. The climatological latent heat flux is, however, too strong over the Gulf Stream in the coupled model. Comparison with an atmosphere-only model reveals that the SST bias of the coupled model leads to the error.
6. Mesoscale Convective Systems over the Rocky Mountains, which contribute to many of the important summertime weather events in the central U.S. are also seen in this simulation, but tend to occur earlier in the year, in spring, and have slower propagation speeds than most observed systems.
7. In common with some previous high-resolution runs [e.g., *McClean et al.*, 2011; *Sakamoto et al.*, 2012], Tropical Cyclones are permitted. The tracks of these extreme events are somewhat realistic except for a striking lack of storms in the N. Atlantic and E. Pacific basins, whilst there are too many strong systems in the western Pacific.
8. The substantial overestimation of Southern Hemisphere summer sea-ice seen in previous CCSM/CESM models is not seen; however, there is a general underestimation of summer sea ice in both high-resolution and standard resolution CESM in the perpetual year 2000 conditions.

Despite these improvements, some limitations of the model simulations persist, such as substantial deep ocean model drift at both high and standard resolutions, excessive precipitation in the ITCZ and wind stress in the extratropical storm tracks, and an overdiffuse Equatorial thermocline. Current model development with CESM is aiming to address these issues.

Current and future plans with these simulations include (i) the analysis of Kuroshio Extension variability on interannual to decadal time scales, and the atmospheric circulation response, (ii) investigation of possible compensation between ocean eddy heat transport and atmosphere heat transport, (iii) Southern Ocean variability, including response of the ocean to changing wind stress in a high-resolution coupled system, (iv) ocean near-inertial wave response to strong winds, (v) relationship of extreme events to large-scale modes of variability, (vi) analysis of Tropical Atlantic climate, and (vii) improvement of regridding of winds onto coastal ocean cells for upwelling studies. In addition, different resolution models are being analyzed (including one with 0.25° resolution in atmosphere, 1° in ocean) to more clearly distinguish the role of resolving ocean features versus resolving atmosphere features in the model improvements seen in CESM-H.

Acknowledgments
Funding for the research on this project came from the Department of Energy Office of Biological and Environmental Research, via the Scientific Discovery through Advanced Computing (SCIDAC) project SC0006743, and we also acknowledge the National Science Foundation and the NCAR "Accelerated Scientific Discovery" computer allocation for extensive use of Yellowstone at the NCAR-Wyoming supercomputer center. Dave Hart of the Computational and Information Systems Lab (CISL) gave excellent support for the project, and the CISL group also provided assistance for performing large jobs on the then-new Yellowstone supercomputer. Thank you to Andy Mai for performing part of the simulation, John Truesdale for analysis of Tropical Cyclones, Jim Edwards and Tony Craig for advise on running CESM at high resolution, and Mark Taylor for advice on running the Spectral Element version of CAM. Rich Neale, Andrew Gettelmann, Jack Chen, and Aneesh Subramanian are thanked for providing comments on the Intraseasonal variability section. Lisan Yu and Xiangze Jin kindly provided access to 0.25° OAFLUX data. James Booth shared analysis of the ERA-Interim storm tracks. Two anonymous reviewers are thanked for their constructive criticism which helped strengthen the paper. The model simulation data from CESM-H are available to the public, at the Earth System Grid, on the webpage http://www.earthsystemgrid.org/. The animations of MCS over the Rockies and of latent heat flux over SST, both using hourly data, can be found on YouTube at https://www.youtube.com/playlist?list=PL5BdpEleiG4Boo-JCGr_34WmnNf9tt4wn.

References

Alexander, M. A., I. Bladé, M. Newman, J. R. Lanzante, N.-C. Lau, and J. D. Scott (2002), The atmospheric bridge: The influence of ENSO teleconnections on air–sea interaction over the global oceans, *J. Clim.*, *15*, 2205–2231.
Bacmeister, J. T., M. F. Wehner, R. B. Neale, A. Gettelman, C. Hannay, P. H. Lauritzen, J. M. Caron, and J. E. Truesdale (2014), Exploratory high-resolution climate simulations using the Community Atmosphere Model (CAM), *J. Clim.*, *27*, 3073–3099.
Balmaseda, M. A., K. E. Trenberth, and E. Källén (2013), Distinctive climate signals in reanalysis of global ocean heat content, *Geophys. Res. Lett.*, *40*, 1754–1759, doi:10.1002/grl.50382.
Bellenger, H., E. Guilyardi, J. Leloup, M. Lengaigne, and J. Vialard (2014), ENSO representation in climate models: from CMIP3 to CMIP5, *Clim. Dyn.*, *42*, 1999–2018.
Bishop, S. P., and F. O. Bryan (2013), A comparison of mesoscale eddy heat fluxes from observations and a high-resolution ocean model simulation of the Kuroshio Extension, *J. Phys. Oceanogr.*, *43*, 2563–2570.
Booth, J. F., L. Thompson, J. Patoux, K. A. Kelly, and S. Dickinson (2010), The signature of midlatitude tropospheric storm tracks in the surface winds, *J. Clim.*, *23*, 1160–1174.
Booth, J. F., L. Thompson, J. Patoux, and K. A. Kelly (2012), Sensitivity of midlatitude storm intensification to perturbations in the sea surface temperature near the Gulf Stream, *Mon. Weather Rev.*, *140*, 1241–1256.
Bryan, F. O., M. Hecht, and R. D. Smith (2007), Resolution convergence and sensitivity studies with North Atlantic circulation models. Part I: The western boundary current system, *Ocean Modell.*, *16*, 141–159.
Bryan, F. O., R. Tomas, J. M. Dennis, D. B. Chelton, N. G. Loeb, and J. L. McClean (2010), Frontal scale air-sea interaction in high-resolution coupled climate models, *J. Clim.*, *23*, 6277–6291.
Burgman, R. J., P. S. Schopf, and B. P. Kirtman (2008), Decadal modulation of ENSO in a hybrid coupled model, *J. Clim.*, *21*, 5482–5500.
Carbone, R., J. Tuttle, D. Ahijevych, and S. Trier (2002), Inferences of predictability associate with warm season precipitation episodes, *J. Atmos. Sci.*, *59*, 2033–2056.

Chang, C.-Y., J. A. Carton, S. A. Grodsky, and S. Nigam (2007), Seasonal climate of the Tropical Atlantic sector in the NCAR Community Climate System Model 3: Error structure and probable causes of errors, *J. Clim.*, *20*, 1053–1070.
Chang, P. (1994), A study of the seasonal cycle of sea surface temperature in the tropical Pacific Ocean using reduced gravity models, *J. Geophys. Res.*, *99*, 7725–7741.
Chelton, D. B., M. G. Schlax, M. H. Freilich, and R. F. Milliff (2004), Satellite measurements reveal persistent small-scale features in ocean winds, *Science*, *303*, 978–983.
Compo, G. P., et al. (2011), The twentieth century reanalysis project, *Q. J. R. Meteorol. Soc.*, *137*, 1–28.
Cook, K. H., G. A. Meehl, and J. M. Arblaster (2012), Monsoon regimes and processes in CCSM4. Part II: African and American monsoon systems, *J. Clim.*, *25*, 2609–2621.
Cunningham, S. A., S. G. Alderson, B. A. King, and M. A. Brandon (2003), Transport and variability of the Antarctic Circumpolar Current in Drake Passage, *J. Geophys. Res.*, *108*(C5), 8084, doi:10.1029/2001JC001147.
Danabasoglu, G., W. G. Large, J. J. Tribbia, P. R. Gent, B. P. Briegleb, and J. C. McWilliams (2006), Diurnal coupling in the tropical oceans of CCSM3, *J. Clim.*, *19*, 2347–2365.
Davey, M. K., et al. (2002), STOIC: A study of coupled model climatology and variability in tropical ocean regions, *Clim. Dyn.*, *18*, 403–420.
Delworth, T. L., et al. (2012), Simulated climate change in the GFDL CM2.5 high-resolution coupled climate model, *J. Clim.*, *25*, 2755–2781.
Dennis, J., J. Edwards, K. J. Evans, O. N. Guba, P. H. Lauritzen, A. Mirin, A. St.-Cyr, M. Taylor, and P. H. Worley (2012), CAM-SE: A scalable spectral element dynamical core for the community atmosphere model, *Int. J. High Performance Comput. Appl.*, *26*, 74–89, doi:10.1177/1094342011428142.
Deser, C., S. Wahl, and J. J. Bates (1993), The influence of sea surface temperature gradients on stratiform cloudiness along the equatorial front in the Pacific Ocean, *J. Clim.*, *6*, 1172–1180.
Deser, C., A. S. Phillips, R. A. Tomas, Y. M. Okumara, M. A. Alexander, A. Capotondi, J. D. Scott, Y.-O. Kwon, and M. Ohba (2012), ENSO and Pacific decadal variability in the Community Climate System Model version 4, *J. Clim.*, *25*, 2622–2651.
Dijkstra, H. A., and D. J. Neelin (1995), Ocean-atmosphere interaction and the tropical climatology. Part II: Why the Pacific cold tongue is in the east, *J. Clim.*, *8*, 1343–1359.
Donohue, K., et al. (2008), Program studies the Kuroshio extension, *Eos Trans. AGU*, *89*, 161–162.
Ducet, N., and P. Y. Le-Traon (2001), A comparison of surface eddy kinetic energy and Reynolds stresses in the Gulf Stream and the Kuroshio Current systems from merged TOPEX/Poseidon and ERS-1/2 altimetric data, *J. Geophys. Res.*, *106*, 16,603–16,622.
Fedorov, A. V., and S. G. Philander (2001), A stability analysis of the tropical ocean-atmosphere interactions: Bridging measurements and theory for El Niño, *J. Clim.*, *14*, 3086–3101.
Fox-Kemper, B., R. Ferrari, and R. Hallberg (2008), Parameterization of mixed layer eddies. Part I: Theory and diagnosis, *J. Phys. Oceanogr.*, *38*, 1145–1165.
Gent, P. R., S. G. Yeager, R. B. Neale, S. Levis, and D. A. Bailey (2010), Improvements in a half degree atmosphere/land version of the CCSM, *Clim. Dyn.*, *34*, 819–833.
Gent, P. R., et al. (2011), The Community Climate System Model Version 4, *J. Clim.*, *24*, 4973–4991.
Gouretski, V. V., and K. P. Koltermann (2004), WOCE global hydrographic climatology, *Tech. Rep. 35/2004*, Ber. des Bundesamtes für Seeschifffahrt und Hydrogr., Hamburg.
Gregg, M. C., T. B. Sanford, and D. P. Winkel (2003), Reduced mixing from the breaking of internal waves in equatorial waters, *Nature*, *422*, 513–515.
Griffies, S. M., et al. (2014), Impacts on ocean heat from transient mesoscale eddies in a hierarchy of climate models, *J. Clim.*, in press.
Grodsky, S. A., J. A. Carton, S. Nigam, and Y. M. Okumura (2012), Tropical Atlantic biases in CCSM4, *J. Clim.*, *25*, 3684–3701.
Guilyardi, E. (2006), El Niño–mean state–seasonal cycle interactions in a multi-model ensemble, *Clim. Dyn.*, *26*, 329–348.
Hansen, J., et al. (2005), Earth's energy imbalance: Confirmation and implications, *Science*, *308*, 1431–1435.
Hoskins, B. (2013), The potential for skill across the range of the seamless weather-climate prediction problem: A stimulus for our science, *Q. J. R. Meteorol. Soc.*, *139*, 573–584.
Huffman, G. J., R. F. Adler, P. Arkin, A. Chang, R. Ferraro, A. Gruber, J. Janowiak, A. McNab, B. Rudolf, and U. Schneider (1997), The Global Precipitation Climatology Project (GPCP) combined precipitation dataset, *Bull. Am. Meteorol. Soc.*, *78*, 5–20.
Huffman, G. J., D. T. Bolvin, E. J. Nelkin, D. B. Wolff, R. F. Adler, G. Gu, Y. Hong, K. P. Bowman, and E. F. Stocker (2007), The TRMM Multisatellite Precipitation Analysis (TMPA): Quasi-global, multiyear, combined-sensor precipitation estimates at fine scales, *J. Hydrometeorol.*, *8*, 38–55.
Hunke, E. C., and W. H. Lipscomb (2008), CICE: The Los Alamos sea ice model user's manual, version 4, *Tech. Rep. LA-CC-06-012*, Los Alamos Natl. Lab., Los Alamos. [Available at http://oceans11.lanl.gov/trac/CICE/attachment/wiki/WikiStart/cicedoc.pdf?format=raw.]
Hurrell, J. W., J. J. Hack, D. Shea, J. M. Caron, and J. Rosinski (2008), A new sea surface temperature and sea ice boundary dataset for the Community Atmosphere Model, *J. Clim.*, *21*, 5145–5153.
Hurrell, J. W., et al. (2013), The Community Earth System Model: A framework for collaborative research, *Bull. Am. Meteorol. Soc.*, *94*, 1339–1360.
Jin, F.-F., J. D. Neelin, and M. Ghil (1994), El Niño on the Devil's Staircase: Annual subharmonic steps to chaos, *Science*, *264*, 70–72.
Jin, X., and L. Yu (2013), Assessing high-resolution analysis of surface heat fluxes in the Gulf Stream region, *J. Geophys. Res. Oceans*, *118*, 5353–5375.doi:10.1002/jgrc.20386.
Jochum, M. (2009), Impact of latitudinal variations in vertical diffusivity on climate simulations, *J. Geophys. Res.*, *114*, C01010, doi:10.1029/2008JC005030.
Jochum, M., and R. Murtugudde (2006), Temperature advection by tropical instability waves, *J. Phys. Oceanogr.*, *36*, 592–605.
Jochum, M., G. Danabasoglu, M. Holland, Y.-O. Kwon, and W. G. Large (2008), Ocean viscosity and climate, *J. Geophys. Res.*, *113*, C06017, doi:10.1029/2007JC004515.
Joyce, T. M., Y.-O. Kwon, and L. Yu (2009), On the Relationship between Synoptic Wintertime Atmospheric Variability and Path Shifts in the Gulf Stream and the Kuroshio Extension, *J. Clim.*, *22*, 3177–3192.
Kunzow, T., et al. (2010), Seasonal variability of the Atlantic meridional overturning circulation at 26.5°N, *J. Clim.*, *23*, 5678–5698.
Kara, A. B., A. J. Wallcraft, and H. E. Huelbert (2007), A correction for land contamination of atmospheric variables near land-sea boundaries, *J. Phys. Oceanogr.*, *37*, 803–818.
Kay, J. E., et al. (2012), Exposing global cloud biases in the Community Atmosphere Model (CAM) using satellite observations and their corresponding instrument simulators, *J. Clim.*, *25*, 5190–5207.
Kelly, K., R. J. Small, R. M. Samelson, B. Qiu, T. Joyce, Y.-O. Kwon, and M. Cronin (2010), Western boundary currents and Frontal Air-Sea Interaction: Gulf Stream and Kuroshio extension, *J. Clim.*, *23*, 5644–5667.

Kirtman, B. P., and P. S. Schopf (1998), Decadal variability in ENSO predictability and prediction, *J. Clim.*, *11*, 2804–2822.
Kirtman, B. P., et al. (2012), Impact of ocean model resolution on CCSM climate simulations, *Clim. Dyn.*, *39*, 1303–1328.
Knapp, K. R., M. C. Kruk, D. H. Levinson, H. J. Diamond, and C. J. Neumann (2010), The International Best Track Archive for Climate Stewardship (IBTrACS), *Bull. Am. Meteorol. Soc.*, *91*, 363–376.
Kwon, Y.-O., M. A. Alexander, N. A. Bond, C. Frankignoul, H. Nakamura, B. Qiu, and L. Thompson (2010), Role of the Gulf Stream and Kuroshio–Oyashio systems in large-scale atmosphere–ocean interaction: A review, *J. Clim.*, *23*, 3249–3281.
Laing, A., and J. Fritsch (1997), The global population of mesoscale convective complexes, *Mon. Weather Rev.*, *128*, 2756–2776.
Large, W. G., and G. Danabasoglu (2006), Attribution and impacts of upper-ocean biases in CCSM3, *J. Clim.*, *19*, 2325–2346.
Large, W. G., and S. G. Yeager (2009), The global climatology of an interannually varying air-sea flux data set, *Clim. Dyn.*, *33*, 341–364.
Lawrence, D. M., et al. (2011), Parameterization improvements and functional and structural advances in version 4 of the Community Land Model, *J. Adv. Model. Earth Syst.*, *3*, M03001, doi:10.1029/2011MS000045.
Levitus, S., T. P. Boyer, M. E. Conkright, D. Johnson, T. O'Brien, J. Antonov, C. Stephens, and R. Gelfeld (1998), *Introduction*, vol. 1, *World Ocean Database 1998, NOAA Atlas NESDIS 18*, 346 pp, U.S. Gov. Print. Off., Washington, D. C.
Lindzen, R. S., and M. Fox-Rabinovitz (1989), Consistent vertical and horizontal resolution, *Mon. Weather Rev.*, *117*, 2575–2583.
Loeb, N. G., J. M. Lyman, G. C. Johnson, R. P. Allan, D. R. Doelling, T. Wong, B. J. Soden, and G. L. Stephens (2012), Observed changes in top-of-the-atmosphere radiation and upper-ocean heating consistent within uncertainty, *Nat. Geosci.*, *5*, 110–113.
Ma, C.-C., C. R. Mechoso, A. W. Robertson, and A. Arakawa (1996), Peruvian stratus clouds and the tropical Pacific circulation: A coupled ocean-atmosphere GCM study, *J. Clim.*, *9*, 1635–1645.
MacKinnon, J. (2013), Mountain waves in the deep ocean, *Nature*, *501*, 321–322.
McClean, J., et al. (2011), A prototype two-decade fully-coupled fine-resolution CCSM simulation, *Ocean Model.*, *39*, 10–30.
Medeiros, B., D. L. Williamson, C. Hannay, and J. G. Olsen (2012), Southeast Pacific stratocumulus in the Community Atmosphere Model, *J. Clim.*, *25*, 6175–6192.
Meehl, G., W. Washington, J. Arblaster, A. Hu, H. Teng, J. Kay, A. Gettelman, D. Lawrence, B. Sanderson, and W. Strand (2013), Climate change projections in CESM1(CAM5) compared to CCSM4, *J. Clim.*, *26*, 6287–6308.
Meehl, G. A., P. R. Gent, J. M. Arblaster, B. L. Otto-Bleisner, E. C. Brady, and A. Craig (2001), Factors that affect the amplitude of El Nino in global coupled models, *Clim. Dyn.*, *17*, 515–526.
Mishra, S. K., M. A. Taylor, R. D. Nair, P. H. Lauritzen, H. M. Tufo, and J. J. Tribbia (2011), Evaluation of the HOMME dynamical core in the aquaplanet configuration of NCAR CAM4: Rainfall, *J. Clim.*, *24*, 4037–4055.
Muñoz, E., W. Weijer, S. A. Grodsky, S. C. Bates, and I. Wainer (2012), Mean and variability of the tropical Atlantic Ocean in the CCSM4, *J. Clim.*, *25*, 4860–4882.
Neale, R. B., J. H. Richter, and M. Jochum (2008), The impact of convection on ENSO: From a delayed oscillator to a series of events, *J. Clim.*, *21*, 5904–5924.
Neale, R. B., et al. (2010), Description of the NCAR community atmosphere model (CAM 5.0), *NCAR Tech. Note NCAR/TN-486+ STR*. Natl. Cent. Atmos. Res., Boulder, Colo. [Available at http://www.cesm.ucar.edu/models/cesm1.1/cam/docs/description/cam5_desc.pdf.]
Osborn, T. R. (1980), Estimates of the local rate of vertical diffusion from dissipation measurements, *J. Phys. Oceanogr.*, *10*, 83–89.
Palmer, T. N., F. J. Doblas-Reyes, A. Weisheimer, and M. J. Rodwell (2008), Toward seamless prediction: Calibration of climate change projections using seasonal forecasts, *Bull. Am. Meteorol. Soc.*, *89*, 459–470.
Philander, S. G. H., and R. C. Pacanowski (1981), The oceanic response to cross-equatorial winds (with application to coastal upwelling in low latitudes), *Tellus*, *33*, 201–210.
Pritchard, M., M. Moncrieff, and R. Somerville (2011), Orogenic propagating precipitation systems over the United States in a Global Climate Model with embedded explicit convection, *J. Atmos. Sci.*,*68*, 1821–1840.
Reynolds, R. W., N. A. Rayner, T. M. Smith, D. C. Stokes, and W. Wang (2002), An improved in situ and satellite SST analysis for climate, *J. Clim.*, *15*, 1609–1625.
Reynolds, R. W., T. M. Smith, C. Liu, D. B. Chelton, K. S. Casey, and M. G. Schlax (2007), Daily high-resolution-blended analyses for sea surface temperature, *J. Clim.*, *20*, 5473–5496.
Richter, I., and S.-P. Xie (2008), On the origin of equatorial Atlantic biases in coupled general circulation models, *Clim. Dyn.*, *31*, 587–598.
Richter, J. H., A. Solomon, and J. T. Bacmeister (2014), Effects of vertical resolution and nonorographic gravity wave drag on the simulated climate in the Community Atmosphere Model, version 5, *J. Adv. Model. Earth Syst.*, *6*, 357–383, doi:10.1002/2013MS000303.
Rienecker, M. M., et al. (2011), MERRA: NASA's modern-era retrospective analysis for research and applications, *J. Clim.*, *24*, 3624–364.
Risien, C. M., and D. B. Chelton (2008), A global climatology of surface wind and wind stress fields from eight years of QuikSCAT scatterometer data, *J. Phys. Oceanogr.*, *38*, 2379–2413.
Roberts, M. J., et al. (2009), Impact of resolution on the Tropical Pacific Circulation in a matrix of coupled models, *J. Clim.*, *22*, 2541–2556.
Sakamoto, T. T., et al. (2012), MIROC4h—A new high resolution atmosphere-ocean coupled general circulation model, *J. Meteorol. Soc. Jpn.*, *90*, 325–359.
Sampe, T., and S.-P. Xie (2007), Mapping high winds from space: A global climatology, *Bull. Am. Meteorol. Soc.*, *88*, 1965–1978.
Seo, H., M. Jochum, R. Murtugudde, A. J. Miller, and J. O. Roads (2008), Precipitation from African easterly waves in a Coupled Model of the Tropical Atlantic, *J. Clim.*, *21*, 1417–1431.
Shaffrey, L. C., et al. (2009), U. K. HiGEM: The new U. K. high-resolution global environment model—Model description and basic evaluations, *J. Clim.*, *22*, 1861–1896.
Small, R. J., S.-P. Xie, and J. Hafner (2005), Satellite observations of mesoscale ocean features and copropagating atmospheric surface fields in the tropical belt, *J. Geophys. Res.*, *110*, C02021, doi:10.1029/2004JC002598.
Small, R. J., R. A. Tomas, and F. O. Bryan (2014), Storm track response to Ocean Fronts in a global high-resolution climate model, *Clim. Dyn.*, *43*, 805–828.
Smith, R. D., et al. (2010), The Parallel Ocean Program (POP) reference manual, *Tech. Rep. LAUR-10-01853*, Los Alamos Natl. Lab., Los Alamos. [Available at http://www.cesm.ucar.edu/models/cesm1.0/pop2/doc/sci/POPRefManual.pdf.]
Smith, T. M., and R. W. Reynolds (2005), A global merged land air and sea surface temperature reconstruction based on historical observations (1880–1997), *J. Clim.*, *18*, 2021–2036.
The Climode Group, et al. (2009), The climode field campaign: Observing the cycle of convection and restratification over the Gulf Stream, *Bull. Am. Meteorol. Soc.*, *90*, 1337–1350.
Thompson, L.-A., and Y.-O. Kwon(2010), An enhancement of low-frequency variability in the Kuroshio–Oyashio extension in CCSM3 owing to ocean model biases, *J. Clim.*, *23*, 6221–6233.

Toniazzo, T., and S. Woolnough (2013), Development of warm SST errors in the southern tropical Atlantic in CMIP5 decadal hindcasts [online], *Clim. Dyn.*, doi:10.1007/s00382-013-1691-2.
Trenberth, K. E., and J. M. Caron (2001), Estimates of meridional atmosphere and ocean heat transports, *J. Clim.*, *14*, 3433–3443.
Trenberth, K. E., J. T. Fasullo, and J. Kiehl (2009), Earth's global energy budget, *Bull. Am. Meteorol. Soc.*, *90*, 311–323.
Wahl, S., M. Latif, W. Park, and N. Keenlyside (2011), On the Tropical Atlantic SST warm bias in the Kiel climate model, *Clim. Dyn.*, *36*, 891–906.
Wallace, J. M. (1975), Diurnal variations in precipitation and thunderstorm frequency over the coterminus United States, *Mon. Weather Rev.*,*103*, 406–419.
Wallace, J. M., G.-H. Lim, and M. L. Blackmon (1988), Relationship between cyclone tracks, anticyclone tracks and caroclinic waveguides, *J. Atmos. Sci.*, 45, 439–462.
Wittenberg, A. T. (2009), Are historical records sufficient to constrain ENSO simulations? *Geophys. Res. Lett.*, *36*, L12702, doi: 10.1029/2009GL038710.
Xie, S.-P. (2004), Satellite observations of cool ocean–atmosphere interaction, *Bull. Am. Meteorol. Soc.*, *85*, 195–208.
Young, G. S., and T. D. Sikora (2003), Mesoscale stratocumulus bands caused by Gulf Stream meanders, *Mon. Weather Rev.*, *131*, 2177–2191.
Yu, L., and R. A. Weller (2007), Objectively analyzed air–sea heat fluxes for the global ice-free oceans (1981–2005), *Bull. Am. Meteorol. Soc.*, *88*, 527–539.
Yu, X., and M. J. McPhaden (1999), Seasonal variability in the Equatorial Pacific, *J. Phys. Oceanogr.*, *29*, 925–947.